INSTRUMENTS AND METHODS OF INVESTIGATION

Laser reduction of graphene oxide: local control of material properties

G V Murastov, A A Lipovka, M I Fatkullin, R D Rodriguez, E S Sheremet

Contents

Abstract. We present a detailed analysis of the available data on the laser reduction of graphene oxide (GO). Issues of GO synthesis, structural models, and methods for controlling the properties of the material are considered. The chemical and thermal reduction mechanisms, the two main photoinduced mechanisms for the transformation of dielectric GO films into conducting structures, are described, and their combined effect is illustrated. The impact of laser radiation parameters on the local functionalization of the material, which determines its properties, is critically analyzed. A summary table of the available data on the laser effect on GO is presented. Various applications are outlined, such as electronics, photovoltaics, energy, and flexible sensors, including medical applications. This study systematizes the results presented in the literature and contributes to the further study of the interaction of laser radiation with carbon materials, their transformation, control of properties, and the potential for application in all-carbon electronics.

G V Murastov [(1)], **A A Lipovka** [(2)], **M I Fatkullin** [(3)],
R D Rodriguez [(4)], **E S Sheremet** [(5)]
National Research Tomsk Polytechnic University,
prosp. Lenina 30, 634050 Tomsk, Russian Federation
E-mail: [(1)] genboysk@gmail.com, [(2)] aal26@tpu.ru, [(3)] mif1@tpu.ru,
    [(4)] raul@tpu.ru, [(5)] jane.sheremet@gmail.com

1. Introduction

Carbon nanomaterials play an important role in basic modern science and applied research. Thus, the unique properties of graphene, such as optical transparency, high electrical and thermal conductivity, and mechanical stability, have made it one of the most studied materials of the 21st century. To conduct a qualitative analysis of the material and its use in creating real devices, critical factors are the production of high-quality graphene, its transfer and stabilization on various substrates, and control of the band gap [1]. In practice, there are several methods of producing the material, for example, the mechanical splitting of graphite up to a monolayer (graphene) by means of an adhesive (Scotch) tape, implemented experimentally by the Nobel laureates Geim and Novoselov [2]. Technologies of epitaxial growth, silicon carbide temperature annealing, and — currently the most widespread — chemical vapor deposition are also intensely used [3–5].

There is also another approach consisting of graphene surface functionalization. In this case, monolayer and multiple-layer carbon films are deposited on various substrates with a subsequent reduction in the graphene monolayer structure by removing earlier attached molecules, groups, and radicals. Notably, surface activation by oxygenic groups ($-COOH$, $-OH$, $= O$, etc.) allowed obtaining a unique material, graphene oxide (GO), which then became a separate subject of study. It is possible to control the GO properties by controlling the reduction process, which implies selective removal of earlier attached groups over the surface of graphene oxide flakes under an external impact. The theoretical ultimate case of GO reduction is graphene, but still with a high concentration of defects; therefore, this

material is called reduced graphene oxide (RGO). Currently, the following approaches to GO reduction are common: heating at a temperature above 200 °C, using chemical reducing agents such as hydrazine and its compounds, and exposure to photons. Less frequently used are exposure to ions, electrons, and electric current action [6].

The laser reduction of graphene oxide is becoming more and more widespread and has a number of advantages over other methods, namely, ecological compatibility, simplicity and scalability of the technology, low cost, and the possibility of creating RGO nanosize regions. Moreover, in this case, toxic chemicals or long-term heating are no longer necessary. Direct impact of a laser beam allows creating complex spatial patterns without the necessity of making lithographic masks. A similar microelectronics fabrication process is exploited in laser lithography using photoresists. The laser reduction method is also quite compatible with rolling technologies both for the deposition of GO films and for their in-line reduction. As drawbacks of laser reduction, we can mention the lengthy processing of large areas, especially with nanometer scanning steps, the incomplete removal of oxygenic groups, and the formation of CO and CO_2 gases in the process of irradiation. The main limitations on the method's spread are due to the laser system itself (control of wavelength, pulse duration, laser pulse power and pulse repetition rate, beam-scanning system). The laser method is applicable both to monolayers and to multilayer GO films, as long as the uniformity of the reduction conditions over depth holds. For few-layer RGO films, some applications have already been pointed out, such as field-effect transistors, light-emitting diodes and molecular sensors. Multilayer films are more frequently used in supercapacitors and other applications requiring a large surface area. In some cases, such an approach allows designing 3D structures with the degree of GO reduction varying over the depth.

In the literature, a huge amount of data has been accumulated on graphene oxide reduction, including a small part devoted to the method of laser reduction. Thus, the search query 'graphene oxide reduction' as of the writing of this paper produced 33,929 publications, whereas 'laser reduction of graphene oxide/graphene oxide laser reduction' brings 30 times less publications (about 1060). The small percentage of publications on the topic is due to the relative novelty of the method: one of the first important papers was published only in 2010 [7], after which the number of publications began to grow rapidly. When using a laser, it is important that the result of reduction strongly depends on many factors, such as the radiation wavelength, pulse duration, laser pulse power, thickness of the graphene oxide film, and suspension concentration. However, the disconnected data obtained by different teams all over the world need systematization, as well as approaches to determine the degree of the obtained RGO film reduction. In addition, there are blind spots in the understanding of the fundamental mechanism, for instance, the assessment of the effect and role of photothermal and photochemical reduction mechanisms.

The currently available review articles, both in Russian [3] and in foreign languages [6, 8–11], do not cover the existing volume of relevant research. The purpose of this paper is to highlight the principles and approaches of GO laser reduction and systematize the literature data. Particular attention is paid to the reduction mechanism and the influence of laser parameters on the resulting structures.

2. Graphene oxide, its structural model, and methods of reduction

2.1 Brief history of graphene oxide

Allotropes of carbon, such as graphite and carbon nanotubes, are united by one factor — their main building block is graphene. Graphene is a monolayer of carbon atoms in the sp^2-hybridization state forming a hexagonal crystal lattice. The first theoretical predictions of the prospect of graphene date back to 1947 [12]; however, it became widely publicized after its experimental discovery almost 60 years later [2]. In spite of the unique properties of graphene — the high mobility of charges and the heat conductivity, optical transparency, and mechanical strength — its application for solving some technological problems can be difficult. In particular, graphene poorly disperses in solvents [13], except some toxic ones or some with a high boiling temperature; it also poorly integrates into polymer structures, which can become a limitation for application in flexible electronics.

At present, a solution is graphene surface 'activation' by a number of functional groups [14], and one of the prospective materials for many applications in electronics is graphene oxide (GO), obtained by graphene oxidation during graphite exfoliation. According to Refs [15, 16], the active centers for attaching hydroxyl (OH), epoxy $(C-O-C)$, ketone (R_1-CO-R_2), carbonyl $(C=O)$, and carboxyl (COOH) groups are defect structures and edge inhomogeneities in graphene plates. Thanks to such embellishments, it is possible to form stable suspensions in water and other solvents (ethanol, ethylene glycol, dimethylformamide, etc.) [17]. In turn, during the sedimentation of multilayer GO films, the separations between monolayers are 0.7–1.2 nm, as compared to 0.3 nm in graphite. This is due to the presence of water molecules between the carbon layers, the distribution of oxygenic groups over the surface, and a defect bending the graphene layer. All of these affect the electric properties of the material. Carbonyl and carboxyl groups make a particular contribution to the GO hydrophilic nature. The presence of certain groups and their quantitative content, the ratio of elements C:O:H, can substantially differ depending on the methods and conditions of synthesis [18].

GO was probably first obtained by graphite oxidation in $KClO_3/HNO_3$ back in 1855 [19]. Unfortunately, methods of analysis at that time did not allow reliable determination of carbon monolayers. Therefore, up to the 21st century, it is possible to find mention of only graphite oxide. In the 20th century, the methods of graphite oxide synthesis were developed by Staudenmaier [20] and Hofmann and Hummers [21]. Today, two main modifications of the Hummers method exist: the modified Hummers method [22] and the improved Hummers method [23]. The method is based on the following process: expanded graphite containing no resin or organic fillers and used as a precursor is mixed with sodium permanganate and sulphuric acid at a temperature of about 40–50 °C to form a paste. Since the reaction is exothermic, the synthesis process is carried out in an ice bath. Then, distilled water is poured into the paste and the resulting suspension is filtered using HCl [24].

The key tendencies in the field of efficient GO synthesis are decreasing the synthesis time, replacing toxic reagents or those facilitating the formation of toxic products in the course of chemical reaction, decreasing the number of technological operations and, respectively, the cost of the process, and

increasing the useful product yield [16, 22, 23, 25–27]. According to the data from Refs [28, 29], the improved Hummers method is currently the most widely used in the production of graphene oxide.

2.2 Structural modes of graphene oxide

In parallel with the development of GO synthesis methods, several structural theoretical models of graphene oxide were proposed (Hofmann, Ruess, Scholz–Boehm, Nakajima–Matsuo, Lerf–Klinowski) [30–32]. The very term 'graphene oxide' (GO) denoting a monolayer of a functionalized carbon skeleton (graphene) became used already after the appearance of these studies; however, since the authors presented models for a single layer of carbon, we can rightly speak specifically about the study of GO. Summary data on the structural models of GO are presented in Table 1.

Nowadays, the model proposed by Lerf and Klinowski is commonly accepted. It was specified that carbon has randomly located oxidized areas and regions, where carbon remains nonfunctionalized and retains the sp^2-hybridization state [35]. A study of GO topological defects and thermally reduced high-purity GO using a transmission electron microscope showed that up to 60% of the surface of GO plates can have a graphene hexagonal structure [36]. It is also confirmed by the calculation model of the molecular dynamics of graphene oxide in water, in which the migration of groups over the surface and the formation of 'pure' graphene areas were shown [37].

Methods of GO reduction are mainly aimed at the most complete removal of oxygenic groups. The methods themselves are described in Section 2.3. For example, according to calculations using the methods of classical molecular dynamics for the process of GO thermal reduction at various temperatures, it was shown that the annealing of hydroxyl and epoxide groups leads to the formation of carbonyl and ether groups, the removal of which is impossible without destroying the graphene flakes. In addition, a great number of defects arise in the plane of the carbon lattice [38]. It is interesting that the structural model of a multilayer RGO system can have graphene planes with a small number of defects. Such graphene flakes (in the case of chemical reduction) and stacks (in the case of thermal reduction) are located between two carbon layers, having residual epoxy and hydro groups [39]. This fact explains some limitations of the GO structure reduction to graphene. As to the laser method of GO annealing, according to our paper, at the moment no structural RGO models are found in the literature.

2.3 Methods of graphene oxide reduction

When the oxygenic functional groups are removed, the hybridization of carbon atoms initially in the sp^3 state occurs, and the hexagonal structure in the graphene plane is restored. This is reflected in the change in conductivity, wettability, porosity, and chemical activity of the material. According to experimental data on GO reduction, the obtained material is only 'like' graphene. Most often it is possible to obtain a material in which some residual oxygenic groups are retained, which considerably worsens its properties compared to graphene; however, it allows controlling the band gap width and chemical properties [3]. This material was named 'reduced graphene oxide (RGO).'

Methods of producing RGO from GO can be classified by the source of action on the material [40]: heat flow [41, 42], chemical reducing agent [43, 44], electric current [45], microwave radiation [46], exposure to light [47, 48] (includ-ing laser irradiation [7]), ion exposure [49, 50], electron beam [51–53], X-rays [54], and water electrolysis [55].

From the above list, exposure to heat, laser beam, and chemicals are the most available and widely used methods of producing RGO.

For a long time, the use of chemical reducers, e.g., hydrazine vapors, was considered the most efficient approach. Thus, in Ref. [43], a chain of reactions was demonstrated leading to the replacement of epoxy groups with nitrogen amines and, after their removal, to the formation of a C = C bond. According to theoretical calculations, the main possible reactions of GO with hydrazine have been demonstrated: epoxy and hydroxyl groups over the surface of the carbon lattice, as well as carboxyl groups on defects and the edges of the GO plate, can be easily removed by the effect of hydrazine vapors [56]. However, the epoxy group located in the plane of the carbon lattice forms a more stable oxyalcohol compound. In addition, the ketone and hydroxyl groups at the edges of the lattice are stable. The formation of stable hydrazone complexes is also possible [57].

Hydrazine and its compounds are toxic substances; therefore, in correspondence with the modern trend of using safe and environmentally friendly processes, a search for 'green' GO reducers is being carried out, including those combined with thermal annealing [58]. In this context, widely known reagents are vitamin C [59, 60] and sugar [61], and as to exotic ones, extractions from the Ceylon argan tree, taro [62], and various-leaved spurges [63].

The main drawback of the chemical impact is the possibility of reducing only the entire GO volume, whereas for practical application a local controllable variation in the properties and reduction degree is more valuable [43].

There are chemical methods that solve the local reduction problem, for example, using the electrochemical reaction of water dissociation. In this case, the conducting probe of an atomic force microscope whose tip size is a few nanometers is used as the anode, while the role of the cathode is played by the current-conducting substrate, usually gold. By means of a high-precision positioning mechanism, the probe is moved to a drop of water located on the GO film surface, after which voltage is applied to the electrodes. As a result of the electrochemical reaction, ions are produced, which cause the reduction process. Using this method, conducting patterns with a minimal size of 4 nm were obtained, which is a definite advantage of the method [35, 64, 65]. However, the process requires expensive high-precision equipment and is science-intensive and time-consuming.

The thermal impact on GO films is a more environmentally friendly, cheap, and safe method compared to chemical reduction [66]. In this method, the quality of reduction depends on temperature, the number and type of removed oxygenic groups, heating rate, and atmosphere composition [67]. Using this method, RGO structures were obtained possessing different types of conductivity, which is a breakthrough for application in electronics [68]. However, the thermal method also allows reducing only the entire volume of material.

There are experimental approaches that combine thermal and chemical impacts. For example, the process of solvother-mal (hydrothermal) reduction is implemented by obtaining overheated supercritical water and the accompanying pres-sure increase inside a hermetic container [69]. In this case, water is an environment friendly chemical reduction agent. Another example is multistep reduction with a combination of different methods. For example, reduction using hydrazine followed by thermal annealing at a temperature of 220°C

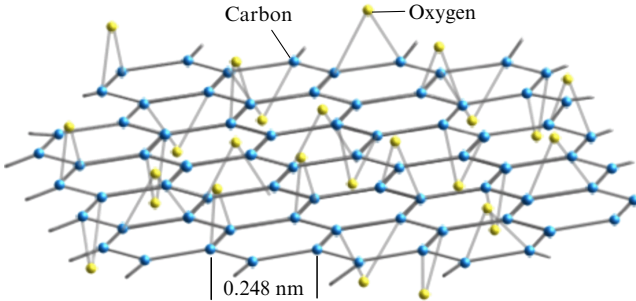**Table 1.** Comparison of graphene oxide skeletal models.

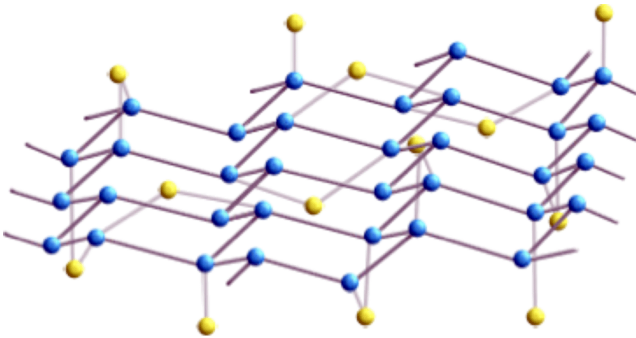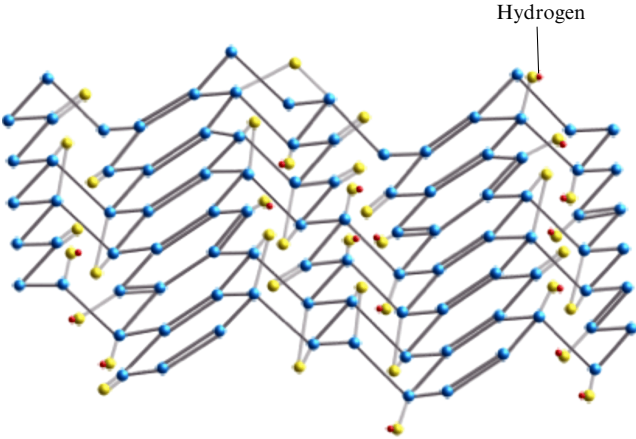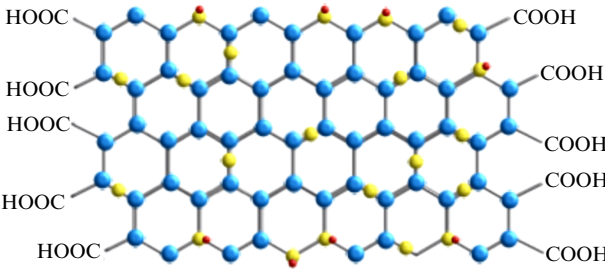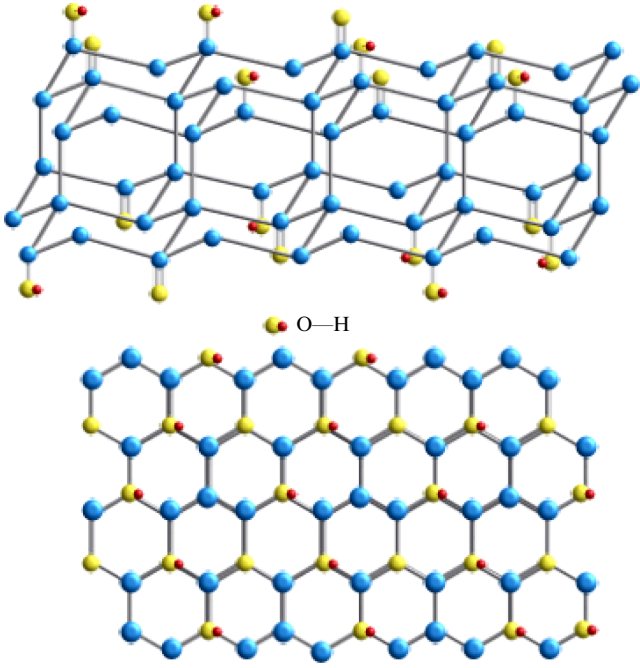| Model name by author	Short description. Characteristics	Schematic representation of the structure	Reference
Hofmann model	Oxygen is bonded to two carbon atoms in a hexagonal lattice through an epoxy bond. Structure is described by ideal formula C_2O.	Carbon — Oxygen 0.248 nm	[31, 32]
Ruess model	Structure has pronounced defects in the plane of the carbon lattice due to trans-conformation, which leads to a wavy structure of graphene. The following functional groups containing oxygen are found in the chemical structure of the model: ether, carboxyl, carbonyl, and hydroxyl. Remaining vacant bonds are occupied by axial $-OH$ groups		[32, 33]
Scholz–Boehm model	Structure shows presence of $C = C$, $C = C$, $C-OH$ bonds and absence of epoxy groups. Concept of the carbon layer as linked ribbons with a rigid quinoid structure.	Hydrogen	[32]
Lerf–Klinowski model	Macro regions containing randomly oriented carbon planes are considered. Planes have flat, unoxidized benzene rings or wavy regions of alicyclic hexatomic rings with $C = C$, $C-OH$ and epoxy groups. Edges contain $C-OH$ and COOH groups.	HOOC, HOOC, HOOC, HOOC, HOOC — COOH, COOH, COOH, COOH, COOH	[30, 32]

Table 1 (continued)

Model name by author	Short description. Characteristics	Schematic representation of the structure	Reference
Nakajima–Matsuo model	Model is based on a two-stage process with the formation of a $(C_2F)_n$-type structure, the presence of $C=O^{\delta-}$, $C^{\delta+}$ bonds, and a charged vacant node point. Model contains at least 2 layers of a carbon matrix linked by a C–C bond at the first stage of 'oxidation' with a transition to the oxide form at the final stage of the process. Model also takes into account the presence of bound and free water in the interlayer space of graphite oxide.	O—H	[32, 34]

allows obtaining structures with greater electric conductivity than GO annealing at a temperature of $550\,^\circ$C. A significant reduction in the annealing temperature allows the use of polymer substrates and creates the prerequisites for obtaining flexible structures [70]. Moreover, reduction with reagents is sufficiently selective, since not all functional groups participate in the reaction. Combining the chemical and thermal impacts, one can reach uniform reduction over the substrate area and increased electric conductivity of RGO [71, 72].

In Section 3, we will consider a method of GP reduction by means of laser radiation and describe the physical principles underlying this process and the specific features of the approach. Among all the above methods of GO reduction, laser radiation impact on suspensions and films is the most environmentally friendly both in terms of the used reagents (e.g., compared with using hydrazine, a toxic and explosive substance) and in terms of energy expenditure (compared to thermal reduction). Moreover, this method is precision-controlled (compared to thermal annealing in furnaces), which allows implementing the reduction locally in the zone of laser beam action. Thus, by scanning the beam over the surface of GO films, one can create patterns with rigorously specified dimensions. The approach can be easily integrated into modern technological processes of photolithography (as opposed to the methods of AFM or SEM lithography, which require complex and expensive instrumentation). For brevity, GO reduced using laser radiation will be referred to below as l-RGO.

3. Laser reduction of graphene oxide

Laser reduction is implemented by irradiating GO films, powders, or suspensions by fluxes of photons with various energies, pulse durations, and power densities. The most widespread technique of exposure is scanning a sample with a focused beam in the XY plane with direct impact of the laser on the surface. Among other methods of pattern formation, especially on GO films, it is possible to single out the imprints of interference patterns on film surfaces when superimposing two coherent beams of light (Fig. 1a). Each point of the pattern reflects the intensity distribution and causes a certain degree of GO reduction. A more compact technique with a Lloyd mirror is also intensely used (Fig. 1e). A configuration with depth scanning is also possible, as shown in Fig. 1b. The main advantage of this scheme is the possibility of creating 3D structures and performing a uniform reduction over the entire film thickness. Also proposed were synchronous and asynchronous irradiation from both sides of the GO film, and reduction and structuring through transparent substrates, which is successfully applied to manufacture multilayer systems in supercapacitors (Fig. 1c and 1d). In systems for fast annealing of large areas, laser beam scanning into a line has been successfully implemented, which allows accelerating the patterning process, as shown for comparison in Fig. 1g. Figure 1f shows a schematic diagram of recording holograms in GO films using an array of microlenses [73–75].

Using various optical schemes experimentally may substantially affect the result; this is exactly why several different irradiation techniques have been realized; however, changes in the source itself and its parameters are more critical for the result of reduction. For a fundamental understanding of the processes occurring under irradiation and further application of the obtained l-RGO structures, it is necessary to understand the mechanisms of reduction and the influence of the laser parameters on the quality.

3.1 Mechanisms of graphene oxide reduction
In the present paper, we consider the data on laser reduction of GO, collected from more than a hundred publications. However, not every experimental study provides the physical
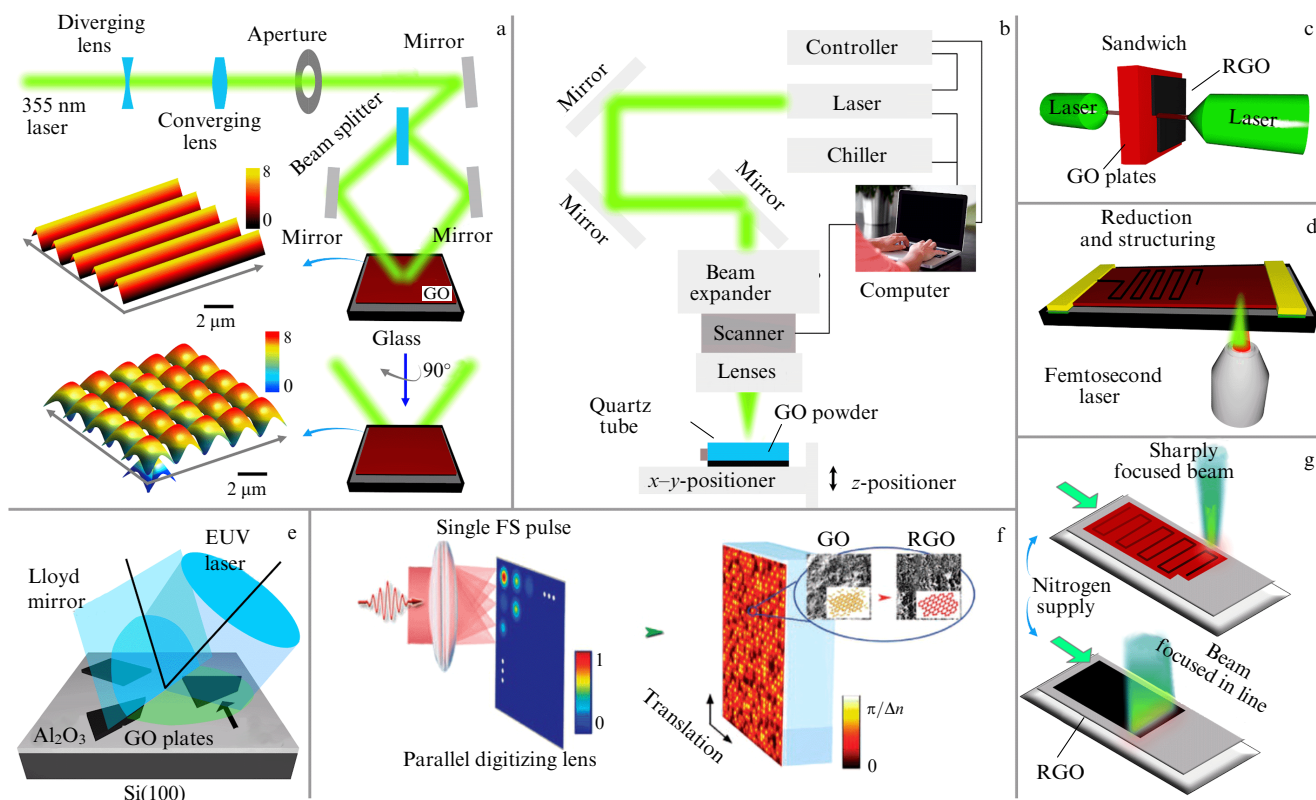
Figure 1. Main methods of irradiating GO with a laser. (a) Combining two interfering beams to obtain uniform parallel fringes from a reduced GO; also, after a rotation of the substrate by 90° and reannealing, it is possible to obtain a netlike conductive structure [75]. (b) Scanning by a focused laser beam of the GO powder in a quartz tube, including depth scanning of the layer [76]. (c) Laser reduction of GO films from both sides [77] and (d) through a transparent substrate [7]. (e) Interference fringes obtained by means of a Lloyd mirror [47]. (f) Recording holograms in the GO structure by means of an array of microlenses [78]. (g) Comparison of GO film annealing point by point and with a laser beam scanned in a line [79].

basis of this process. Based on presently existing theories, it is possible to distinguish three mechanisms leading to laser-induced GO reduction: (1) photochemical action; (2) photo-thermal action; (3) a combination of photochemical and photothermal effects.

3.1.1 Photoreduction (photochemical laser action). The reduction of films and suspensions of 'graphite oxide' (graphene oxide) by light is mainly associated with the detachment of epoxy and hydroxyl groups as a result of absorbing a photon with the formation of CO and CO_2 gases. Under the action of ultraviolet (UV) radiation with the energy of a quantum above 3.2 eV, the change in the hybridization of carbon atoms from sp^3 to sp^2 and the formation of small π-domains also occurs. In this case, a mechanism of migration of oxygenic groups along the graphene nanosheets with a transition into carbonyl, carboxyl, and cyclic (e.g., oxirane, oxetane, 5 and 6-atom fragments) is assumed. Long-term exposure of samples (a few hours) leads to the opening of rings and dissociation of the carbonyl and carboxyl groups. It is noted that the dissociation process is possible in highly excited singlet states and competes with the process of internal conversion [80–82]. These studies were carried out using mercury lamps and filters in a wavelength range of 260–390 nm. It is noteworthy that the impact of white light from a xenon lamp (from 400 nm to near IR) with a power of 450 W on an alcohol suspension of graphite oxide by no means affected the material properties. The reduction of this suspension is possible by introducing a photocatalyst, e.g., titanium or zinc oxide [83, 84].

In turn, the monochromatic radiation from a crypton lamp with a wavelength of 123.6 nm and power density of 1.3 mW cm^{-2} gives rise to a reduction in the concentration of C–O bonds, decreases the water content, and increases the concentration of double bonds of carbon in the film. At the same time, it is noted that the reduction of the GO film occurs mainly due to the cleavage of polar C–O bonds. The process is accompanied by an increase in the density of free electrons at the Fermi level and the growth of graphene clusters, which form continuous chains. Under sufficiently large doses of radiation, these changes lead to the appearance of noticeable conductivity of the order of 1–3.7 S cm^{-1}, which corresponds to the values characteristic of organic semiconductors [85, 86].

Realization of a purely photochemical mechanism of reduction in the infrared (IR) range is possible if the duration of acting laser pulses is not less than 0.37 ps (the experimentally measured time of charge carrier scattering by optical phonons is 0.37 ps and by acoustic phonons, 4.3 ps, whereas the interband recombination time is 67 ps) [87]. For example, to create holograms, GO/CdSe composite films were exposed to single pulses with a duration of 100 fs (source wavelength 800 nm). A schematic diagram of irradiation and luminescence spectra of cadmium selenide nanoparticles with increasing laser beam density are shown in Fig. 2a. In this mode, it is possible to reduce regions whose size is restricted by the diffraction limit of the optical system, since there is no heat diffusion over the volume, which is seen in Fig. 2b. For an aperture equal to 1.2, it was possible to focus the radiation onto a spot 0.55 μm in diameter in the focal plane; in this case, the temperature growth was monitored by the fluorescence
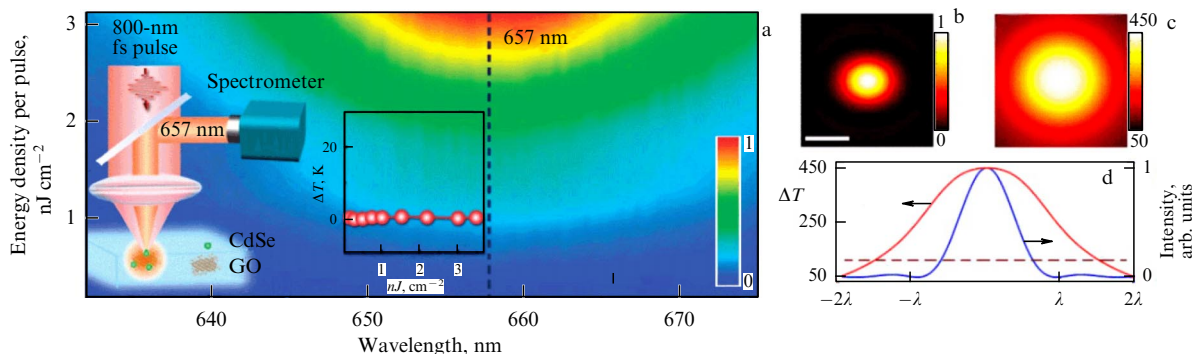
Figure 2. (a) Schematic diagram of the photochemical effect of a laser beam on GO to RGO conversion (inset shows stability of local temperature during the laser operation at a repetition rate of 1 kHz and various values of pulse energy density). Dashed line shows the position of the luminescence peak of CdSe nanoparticles used to assess the heating. Region of GO modification: (b) without significant heating of the film, size is limited by the diffraction limit of the optics, and (c) with thermal impact of the laser due to the temperature growth in the focal plane of the lens with a numerical aperture of 1.2, the energy flux being 5×10^{-10} J cm^{-2} and the exposure time being 10 ms. (d) Comparison of the heating intensity profile in the coordinates of laser wavelength: without heating (photochemical regime) and with the thermal path length taken into account (photothermal regime). Scale for Figs (b) and (c) is 3 μm [78].

spectra of CdSe nanoparticles playing the role of nanothermometers (see inset in Fig. 2a). It is interesting that, when the laser operates at a repetition rate of 1 kHz, no significant heating is detected up to values of the pulse energy density of the order of 4 nJ cm^{-2}. However, in the same interval of energies, a linear growth of temperature is observed, when the repetition rate is increased to 80 MHz. In this mode, the diffraction limit is not attainable because of heat diffusion in the material, which broadens the laser imprint on the film surface (Fig. 2c). A comparison of the reduced region profile for a diffraction-limited spot and under considerable heating is presented in Fig. 2d [78]. This work is a rare example of studying exclusively the photochemical effect under laser reduction of OG.

3.1.2 Heating graphene oxide with light. *Photothermal* action implies graphene oxide heating under the action of a laser, and the key factor is the efficiency of light-to-heat conversion. A model calculation for 6 GO layers under the incident flux power density of 3.4×10^9 W m^{-2} showed that, with a growth in the number of layers, the peak temperature at the spot center has a linear dependence, and for the upper layer the temperature can reach $\sim 500\,^\circ$C in 10 ms (Fig. 3a) [88]. According to other data, the peak temperature when using a high-power nanosecond IR laser can take values in the range of $1200 - 1800\,^\circ$C, and in the center of the laser spot it can exceed these values due to the sharp heating front (Fig. 3b) [89, 90]. Moreover, the last experimental studies show the possibility of heating up to 3500 K [91]. The results of modeling the effect of picosecond pulses are also interesting. In this case, a nonstationary regime takes place, in which for a time of several ten picoseconds a temperature difference between the upper and lower layers is established, reaching $\sim 400 - 800$ K. The modeling was conducted using a 1.2-μm-thick film, the pulse duration was 10 ps, the repetition rate was 100 kHz, the power varied from 7 to 50 mW, and the irradiation was carried out from above. Under these conditions, the system reaches equilibrium within 10^{-8} s, and the peak temperature of the upper layer decreases significantly — to $350 - 400$ K (Fig. 3c).

Hence, the laser exposure of GO films can give rise to a significant heating of both the film surface and the entire structure. Heating to high temperatures leads to GO structural changes: the energy transfer to a bound matrix of carbon and oxygenic groups excites active centers of vibrations in the system, the atoms at the sites of hexagonal graphene lattice change their hybridization, and free radical groups react among themselves and form various gases (e.g., CO_2, CO), tending to leave the material and creating pressure in the system, which is considered one of the main reasons for forming a highly porous carbon material in the process of laser reduction [92].

The process of GO thermal reduction has been studied rather well in the case of controlled heating in furnaces. Qualitatively, the temperature range from room temperature to $2000\,^\circ$C can be divided into five significant subranges, each characterized by certain changes in the structure of the material [93].

(1) Room temperature–130 °C. In this temperature range, the GO layers become closer due to evaporation of free water molecules between the layers and on the surface.

(2) $140 - 180\,^\circ$C. Intense evaporation of water goes on, the process of GO flake layering partially occurs with the intense expelling of gases, which strongly affects the structure porosity.

(3) $180 - 600\,^\circ$C. Removal of carboxyl and hydroxyl groups, formation of CO and CO_2 gases.

(4) $600 - 1000\,^\circ$C. Accumulation of defects in the carbon lattice upon destruction of epoxy groups; the cleavage of C–C bonds is possible, due to which the graphene plane becomes more even. GO annealing above 600 °C is carried out in an inert environment to prevent burning of both films and powders.

(5) $1000\,^\circ$C and higher. The number of defects in the carbon lattice decreases, the layers become more oriented and closely spaced, and the structure is more and more graphene-like. With the growth of temperature, the probability of formation of covalent bonds between carbon atoms increases, i.e., the reconstruction of hexagonal lattice occurs (Fig. 3d) [91]. The reduction is most efficient at temperatures close to 4000 K.

3.1.3 Chemical reaction and heating under the action of light. The third theory of the *combined effect of photothermal and photochemical exposure* is the most common [94–99]. It is assumed that laser radiation causes a photoinduced chemical process of removing oxygenic groups from the graphene surface, and the heating leads to a conversion of carbon into the graphene sp^2 structure [29]. Practically, it is rather
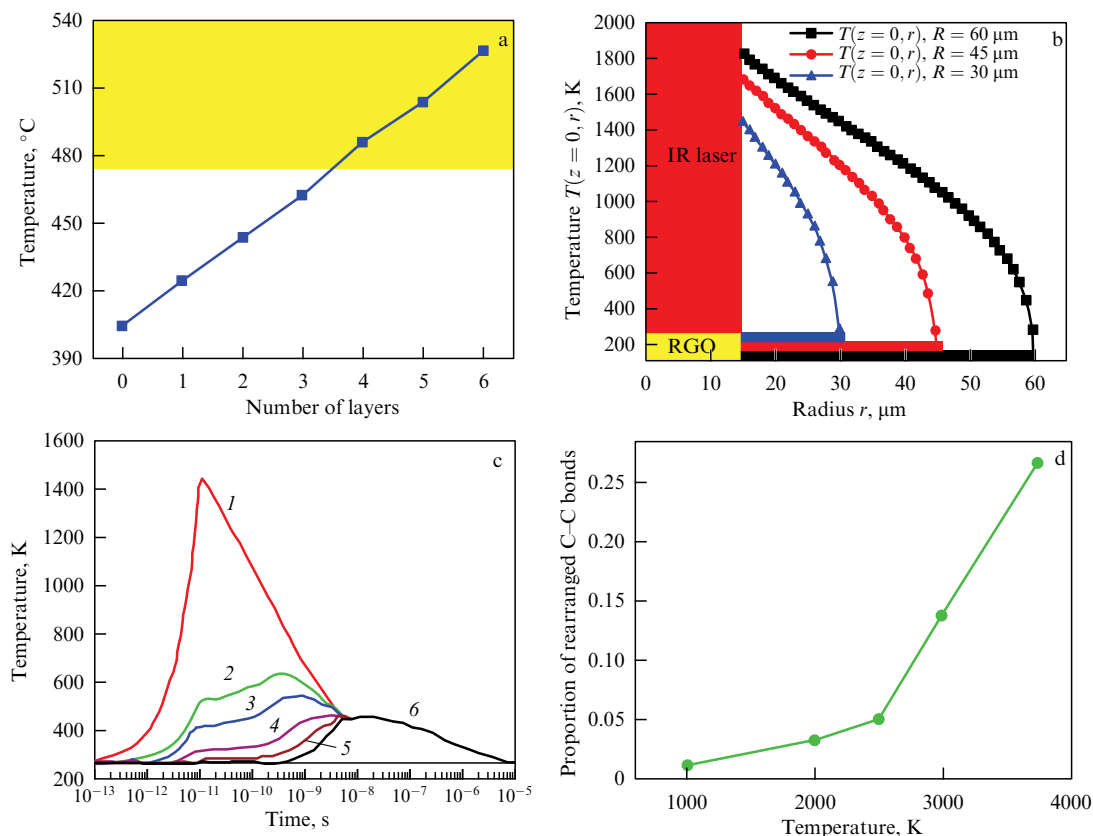
Figure 3. Simulation of the thermal effect of laser irradiation at various parameters: (a) dependences of peak temperature on thickness (number of layers) in GO films at constant irradiation parameters (wavelength 663 nm, power density 3.4×10^9 W m^{-2}, exposure time 10 ms) [88]; (b) model distribution of temperature in the beam action region and along the radius; calculations were performed in cylindrical coordinates for an IR laser of 1064 nm, 200-ns pulse, peak power density 9.62×10^4 W cm^{-2}) and for models of different sizes, 30, 45, and 60 µm, respectively [90]; (c) time scan of the temperature field in a film cut 1.2 µm thick under exposure to picosecond pulses (digits in the plot indicate: *1* — film surface, *2* — 300 nm deeper, *3* — 500 nm deeper, *4* — 700 nm from the surface; *5* — 900 nm, and *6* — interface between the film and the substrate) [89]; (d) reduction of graphene structure at high temperatures of laser impact.

difficult to separate these processes. However, the relative contribution of each mechanism can be controlled within a certain range by regulating the laser power and scanning speed. For example, the content of carbon in hexagonally bound layers at the level of 20.99% remains practically unchanged under low power of the laser source from 3 mW to 13 mW. In this case, the removal of oxygen groups is limited (about 5%) until the laser power reaches 13 mW. At a power of 13 mW, the efficiency of the removal of oxygen groups can be more than doubled [99].

Not only power but also the wavelength of laser radiation can affect the reduction mechanism. The IR effect is mainly considered to be associated with heating, and the UV effect, with photoinduced chemical processes of removing oxygenic groups [96]. It is understood that, in a particular case, one mechanism or another is more responsible for the reduction process, but it is always possible to separate the influence of both in different proportions [94].

The pulse duration also affects the manifestation of mechanisms. For example, the removal of oxygen under the action of a femtosecond laser is associated with electronic excitation and the thermal effect, caused by electron-hole recombination. In the process of laser action, significant excitation of electrons occurs in the first few picoseconds, when an electronic transition to an unbound state occurs. The excitation can substantially weaken C–O bonds at the top of the valence band, thus leading to an instantaneous removal of

oxygen. After the electron-hole recombination (~ 100 ps), the mechanism of thermal reduction dominates [100].

Practical implementation of l-RGO requires taking into account a variety of parameters, such as the reduction degree, porosity, and electric conductivity. The next section is devoted to quality assessment of the obtained structures.

4. Quality assessment of the reduced graphene oxide structure

One of the advantages of reducing GO by means of laser radiation is the possibility of efficiently controlling the local action on films by varying such parameters of the source as the wavelength, energy density, pulse duration, and pulse repetition rate, as well as the composition and condition of the gas environment in which the reduction is carried out [101]. Having analyzed the experience accumulated by various research teams, one can assess the influence of the parameters on the structure and properties of l-RGO, as well as determine the optimal conditions for the formation of the highest-quality structures. However, three problems inevitably arise when systemizing the literature data:

● *there is not enough information in papers* about experimental details (beam cross-section area, duration and repetition rate of pulses, or surface scanning speed) to represent the reduction parameters in a single system, for instance, for calculating power density or energy density;

● there is *no common protocol for preparing samples and GO* (different methods of synthesis and reagents are used to prepare GO, so that the proportions of oxygen and carbon may be different);

● *various external factors and substrate material* affect the obtained structure (gas environments, temperatures, as well as methods of suspension application and drying films on various substrates).

In Section 7, we present a summarizing Table 3 with the results of research on GO laser irradiation under various conditions. It describes the source parameters, substrate material, thickness of deposited GO film, particular conditions of the environment or experiment setting, and the values of conductivity of the obtained structures. The electric conductivity is an important parameter to assess the reduction quality, which determines the field of RGO application. As a rule, to assess l-RGO films, the values of sheet resistance in Ω/sq or specific conductance in S m^{-1} are used.

Table 3 also presents the degree of reduction according to data from Raman spectroscopy (RS) and X-ray photoelectron spectroscopy (XPS) with references to sources. These techniques are the most informative and efficient in the analysis of two-dimensional carbon materials.

XPS allows studying the surface chemistry of carbon materials covering only a surface layer a few nanometers thick. The following spectra are used for the analysis:

— the survey spectrum (0–140 eV) makes it possible to assess the carbon-to-oxygen ratio after reduction, as well as to detect impurities (e.g., sulphur) that can appear in the process of synthesis;

— the C(1s) region ($\sim 282-292$ eV) gives some idea about $C-C$, $C-O$, $C=O$, $O-C=O$ bonds and allows estimating the carbon percentage in these states;

— the O(1s) region ($\sim 528-538$ eV) allows studying $O-C=O$, $C=O$, $C-OH$, $C-O-C$ bonds. GO and RGO contain edge defects, functional groups, which is reflected by the shape and intensity of XPS peaks. The result is affected by the exposure parameters, method of synthesis, and surface state of the GO itself [102, 103].

It is common to distinguish three characteristic bands in the vibrational Raman spectra of GO and RGO:

— the D band (1350 cm^{-1}) — the vibrations of longitudinal and transverse phonons at the edge of the Brillouin zone. In this case, the scattering is due to vibrations with a nonzero wave vector [104]; therefore, the appearance of a D peak is possible only if the graphene has defects;

— the G band (1580 cm^{-1}) — the transverse mode of vibration in the plane of the layers. It is formed due to Raman scattering with the participation of phonons from the Brillouin zone center and is characteristic of graphite and all its derivatives with the sp^2 hybridization;

— the second-order 2D band (2690 cm^{-1}) — its existence is due to the symmetric stretching vibrations of the graphene ring [105].

In contrast to the G peak, the positions of the D and 2D peaks can change, depending on the exciting radiation [106]; therefore, in Table 3, the exciting light wavelength is also presented. From the peak position, half-width, and shape, as well as from the ratio of band intensities, the level of defectiveness, the number of oxygenic groups, and the degree of reduction are assessed. It is also possible to determine the number of carbon layers [107–109]. Moreover, performing the sample surface mapping, the distribution of defect density and the quality of reduction in RGO films are studied [107].

4.1 Effect of power density/energy (threshold phenomena)

Figure 4 illustrates the results of XPS and Raman spectroscopy for l-RGO depending on two parameters: laser wavelength and energy density. The data are collected from literature sources, presented in Section 7, Table 3. Figure 4a shows that the maximum value of the C/O ratio corresponds to the UV spectral region and the energy density up to 100 mJ cm^{-2}. Apparently, this is associated with the efficient removal of oxygenic groups upon absorption of high-energy photons. In turn, the intensity ratio of the D and G peaks carries information about the concentration of defects in the graphene crystal lattice (Fig. 4b). The minimum value falls in the red and IR spectrum ranges, and the power density can be much higher than 100 mJ cm^{-2}, which does not contradict the XPS data, since in this case the concentration of crystal lattice defects is meant, rather than merely the presence of oxygenic groups. However, at a large concentration of defects, this ratio becomes insensitive to structure changes. Therefore, the ratio of two other peaks has been evaluated (I_{2D}/I_G), showing the distribution of the reduction degree in the visible and UV ranges with higher quality (Fig. 4c).

It is necessary to note the systematization 'white spots' in the plots presented. The black regions in Fig. 4b, c indicate the partial absence of information in the literature. This is because there is no single approach to the analysis of l-RGO and there are no necessary data in many papers for carrying out a complete statistical analysis. In addition, in the Raman scattering data, a large spread is observed, which indicates a
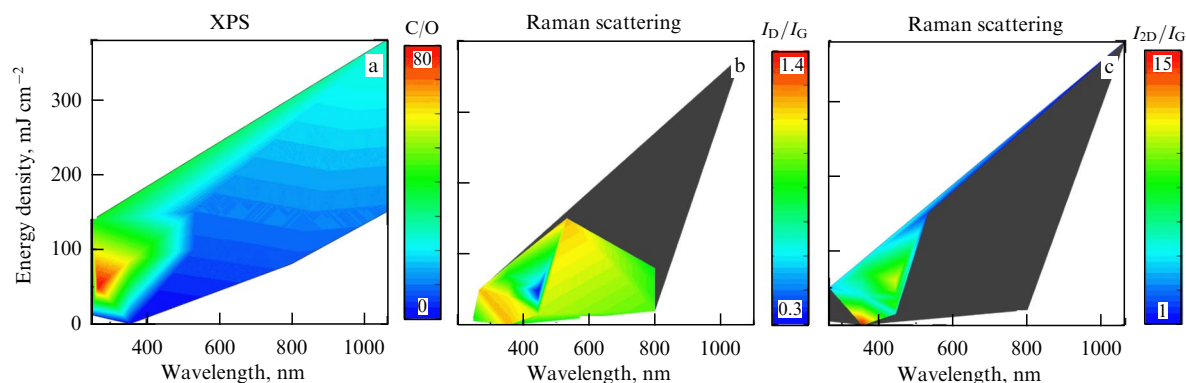

Figure 4. Degree of GO reduction according to data from XPS (a) and Raman scattering (b, c), depending on the parameters of the applied laser source. Black area shows the absence of data in the literature sources. Data are taken from papers systemized in Table 3 and Section 7.
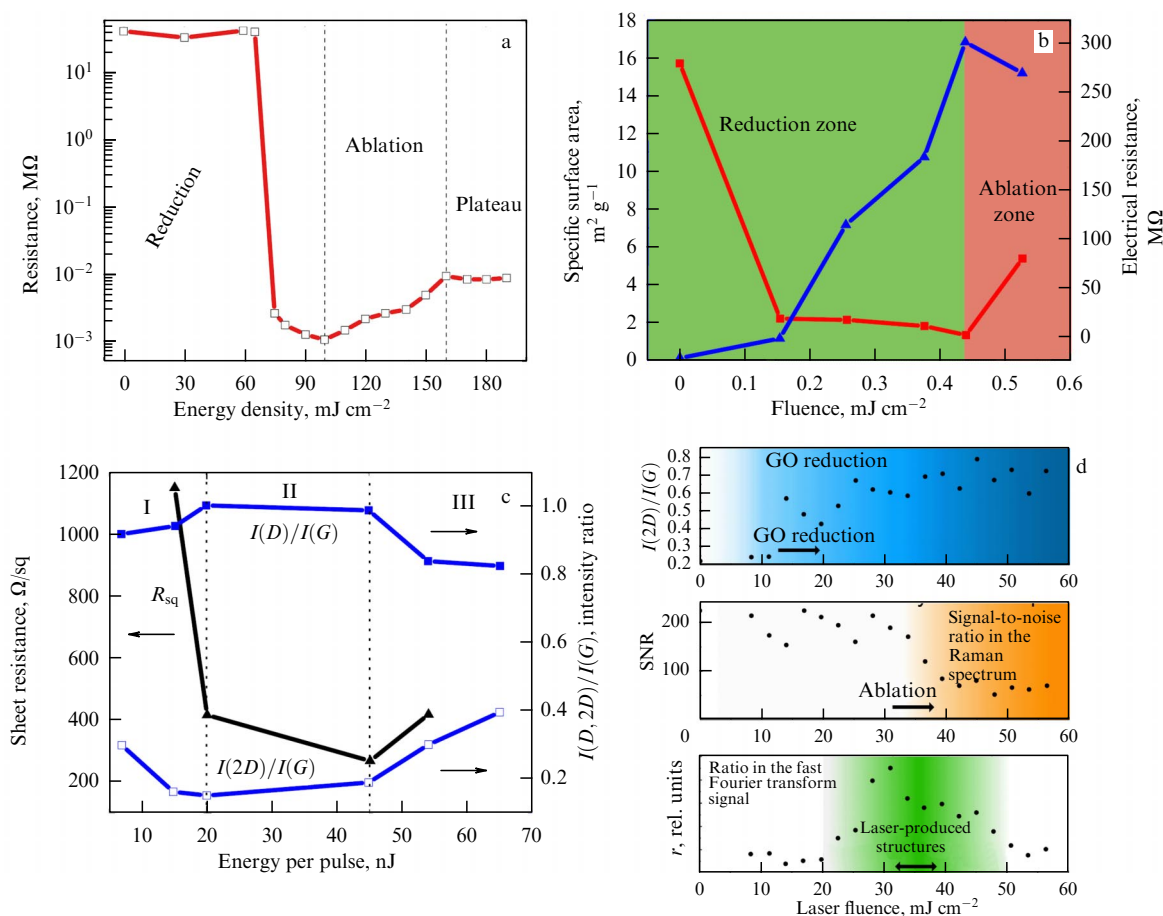
Figure 5. Threshold effect of laser action on graphene oxide with the following source parameters: (a) 248 nm, 20 ns [113], (b) 355 nm [79], (c) 515 nm, 280 fs [114], (d) 1030 nm, 280 fs [115].

different degree of reduction of the crystal lattice structure. To minimize the spread, it is necessary to take into account a variety of parameters, such as the scanning speed, processing time, duration of pulse action and pause between pulses, difference in synthesis methods, sample preparation, substrate material, external gas environment, overlap area, and even speed of blow-off used for heat removal. Such are indeed the parameters that generally determine the dynamics of heating and cooling of the material, the fraction of absorbed radiation, and, finally, the properties of l-RGO.

Moreover, in addition to the reduction itself, the production of l-RGO can be accompanied by material ablation [110], burning, redeposition of the substance, and other phenomena, implying a threshold character of the dependence on the power density [111, 112]. Figure 5 summarizes the available information about threshold phenomena, using which it is possible to decide in which energy density ranges the reduction will be more efficient and will not lead to material removal. For example, in Ref. [113] (Fig. 5a), it was shown that an increase in the laser energy density from 65 to 75 mJ cm^{-2} leads to a drop in resistance by 4 orders of magnitude and a GO reduction. However, upon a further increase in the energy density, the carbon bonds are violated and material ablation occurs; in this case, a growth of resistance is also observed, until its values reach a plateau at 150 mJ cm^{-2}.

Reference [79] studied the regions of reduction and ablation of GO powders under the action of a UV laser. It was shown that as the fluence of 0.438 mJ cm^{-2} is exceeded, material

ablation occurs, which simultaneously leads to a sharp growth in the electric resistance (Fig. 5b). The reduction mechanism shown in Ref. [114] (Fig. 5c) also exhibits a threshold character. Thus, up to pulse energies of 20 nJ, the dominance of laser photochemical action is noted, while above 45 nJ, the photothermal effect dominates. The interval from 20 to 45 nJ is conditionally considered an interval of combined action, where the resistance remains practically unchanged. A qualitative analysis of Raman spectra of l-RGO films obtained under exposure to femtosecond pulses showed that the reduction begins at the fluence values of 11 mJ cm^{-2}, whereas the ablation begins at 35 mJ cm^{-2} (Fig. 5d).

In the same paper, it was shown that an increase in the number of pulses hitting the same laser spot affects the l-RGO electrical characteristics. Thus, after exposure to 10^4 pulses with a fluence from 11 to 34 mJ cm^{-2}, the sheet resistance was from 0.86 to 2.80 kΩ/sq. When the number of pulses was decreased to 10^2, the resistance increased to 9.7 kΩ/sq [115]. Thus, the power/energy is the key parameter to control reduction and determine the range of parameters at which no material removal, or other phenomena unwanted for high-quality GO reduction, occur. However, this value should be considered only taking into account the other parameters of the source (wavelength, pulse duration, etc.).

4.2 Effect of radiation wavelength and pulse duration
In the present paper, the sampling of laser radiation sources fits the range from 46.9 nm to 10.6 μm, covering the UV, visible, and IR spectral ranges. In most papers, the wave-

lengths 1064 nm, 248 nm, and 405 nm are used (Appendix, Fig. 13). In addition, the pulse durations of different sources may differ by up to 10^{15} times (femtosecond pulses and continuous-wave action, respectively) (Section 7).

To assess the reduction degree and to study processes in the UV region, studies using wavelengths below 400 nm are considered. Thus, the minimum ratio I_D/I_G is 0.56 and, therefore, less defective structures were obtained at $\lambda = 248$ nm [113], and the maximum ratio of 1.44 was obtained at $\lambda = 355$ nm [96]. For the visible range (400–800 nm), the minimum and the maximum values are ~ 4 (632.8 nm [98]) and 0.78 (515 nm [114]), and for IR radiation (above 800 nm), 0.27 (1064 nm [116]) and 2.72 (10.6 μm [92]). The analysis revealed no dependence of the reduction quality on pulse duration because of a large spread in values, which is partially associated with using different feedstock to obtain GO–RGO, as well as with the exciting light wavelength in Raman spectroscopy [98]. However, as a rule, in the studies carried out with femto- and picosecond lasers, the ratio I_D/I_G is more frequently less than 1, and when using longer pulses is it greater than 1. That is, under exposure to shorter pulses, RGO turns out to be less defective due to efficient temperature annealing, leading to the reconstruction of the graphene hexagonal lattice. Such a dependence is also observed upon decreasing the wavelength and, correspondingly, the growth of quantum energy, which is due to the dominance of the photochemical reduction mechanism leading to a decrease in the number of defects and oxygenic groups.

The influence of wavelength on the RGO structure has been systematically studied under exposure to lasers with wavelengths of 266, 355, 532, and 1064 nm, the pulse duration being ~ 6 ns and the rest of the conditions being the same. No direct linear dependence between the C/O ratio and the source wavelength was found. For wavelengths of 266, 355, 532, and 1024 nm, the C/O ratio is 79, 56.47, 10.01, and 25.66, respectively. The maximum content of carbon (99.44%) was found in the sample exposed to light with a wavelength of 1064 nm (the initial content of carbon in the GO was 68.28%). Under the alternating action of two sources at 266 nm and at 1064 nm, the oxygen content of 0.94% in the l-RGO was achieved. The C/O ratio amounted to 105.38 and the I_D/I_G ratio was 0.69. To date, this is the most efficient result of GO reduction under laser impact published in the literature [96].

4.3 Change in graphene oxide film thickness under laser annealing

A number of parallel processes occur during the reduction of GO films, which integrally manifest themselves in the nonlinearity of the observed phenomena. For example, depending on the type of action, both an etch of the film and an increase in its thickness are possible [117]. A decrease in the film thickness is associated with the removal of water molecules and oxygenic groups from the interlayer space, the change in the hybridization state, and burning (ablation) of the upper layers [88], whereas the thickening and porosity increase are associated with gas expulsion, RGO redeposition, and splitting of carbon layers.

Under exposure to a laser beam with a wavelength of 532 nm, a decrease in the GO film thickness by 5 nm and 15 nm is observed (the initial thickness being 15 and 32 nm, respectively). When using high-intensity radiation with thick films, such compression is explained by the removal of GO layers and partial reduction of the rest film. In thin films, light

absorption and structure heating are smaller, but sufficient for thermal GO reduction and compressing the film without ablation (as shown in Fig. 6) [118].

The film thickness can be modulated by changing the radiation power and scanning speed. In such a way, l-RGO films 22 nm and 72 nm thick were obtained at the initial GO thickness of 110 nm. In turn, slow surface scanning leads to a greater influence of the thermal effect and to possible ablation of the material. The dependence of film thickness on the energy density is presented in Fig. 6b. It is interesting that, upon an increase in energy per unit area, a transition to the saturation regime occurs (at the energy density of 37.5 mJ cm^{-2}, wavelength of 780 nm, and pulse duration of 70 fs). Above this value, a loss of thickness is barely observed [99].

Changing the pulse duration also significantly affects the RGO film morphology. Thus, under the action of femtosecond pulses, the film acquired a silver-to-white color and was hardly deformed, staying on the substrate. On the contrary, the use of nanosecond pulses leads to deformation — to the appearance of mounds, detaching of the film from the substrate, and — when irradiating the RGO regions previously reduced by femtosecond pulses — to partial ablation of the material [114]. It was also revealed that, under the action of short femtosecond pulses on a GO film, the formation of a shock wave is possible, caused by the effect of light pressure. The propagation of the wave through the film volume ensures rearrangement of atoms, i.e., GO reduction [7]. In addition, material etch is clearly traced when increasing the irradiation power.

An opposite effect is observed when using carbon dioxide lasers (9.6 and 10.6 μm). The impact on GO films (from 6 to 22 μm tick) leads to thermal expansion by a few orders of magnitude (Fig. 7a). Such vast cracking/splitting of graphene layers is explained by an instantaneous intense gas release caused by the laser radiation. The pressure created by water vapors and oxygen release is the main course of the appearance of such micropores, cracks, and cavities in the film [76, 77, 92, 119]. This effect is observed independent of the radiation wavelength (248 nm [120], 405 nm [121], 1.06 μm [77, 101], 10.6 μm [77]), although it manifests itself to a lesser degree when using lasers with a long pulse duration (nanosecond and microsecond ranges), where the photothermal mechanism apparently dominates. The increase in the film thickness shown in several papers, mentioned above, is summarized in Figs 7b–d

During exposure to $\lambda = 650$ nm in three different ranges of power, three different physical processes were shown with the formation of different structures: RGO growth (1.1–11.5 mW), a transition region (71–116 mW), and an etch region (> 172 mW) (Fig. 8) [112]. In the first case, the change in the material's color, increase in film thickness (explained by gasification), and transmission of GO into l-ROG are observed. Upon an increase in power in the transmission region, alongside gas extrusion are a reduction and layer-by-layer etching of GO, due to which the l-RGO thickness becomes smaller. At high powers, it is possible to achieve ablation of all GO layers; in this case, clearly expressed l-RGO regions stay at the edges, because, due to the Gaussian energy distribution in the laser spot, the intensity is much smaller at the edges [110].

Thus, it is possible to distinguish the following versions of processes occurring in GO films under exposure to laser radiation:
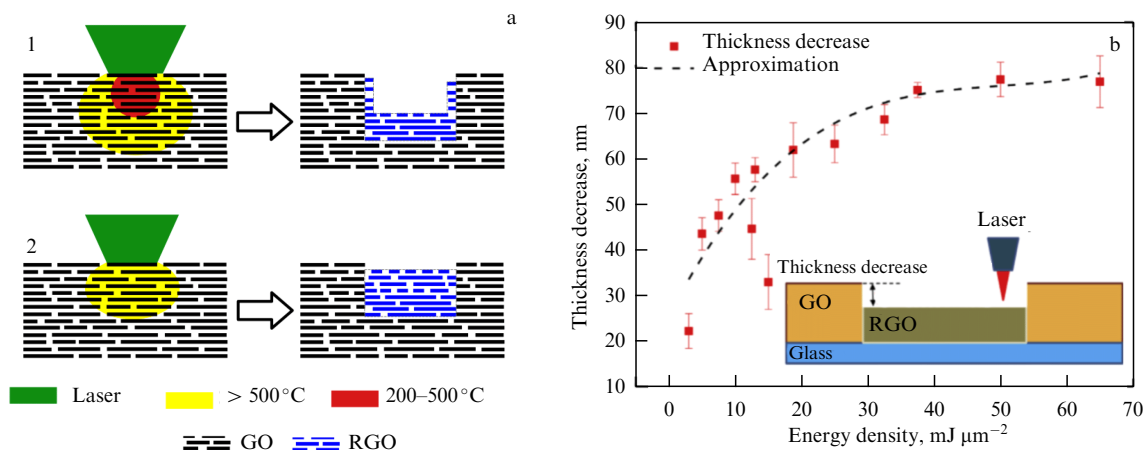
Figure 6. (a) Schematic representation of the mechanism of film thickness decrease [118]. (b) Decreasing the GO film thickness in the process of laser processing. Presented dependence shows how the film thickness changes when increasing the energy density in the beam (wavelength 780 nm) [99].
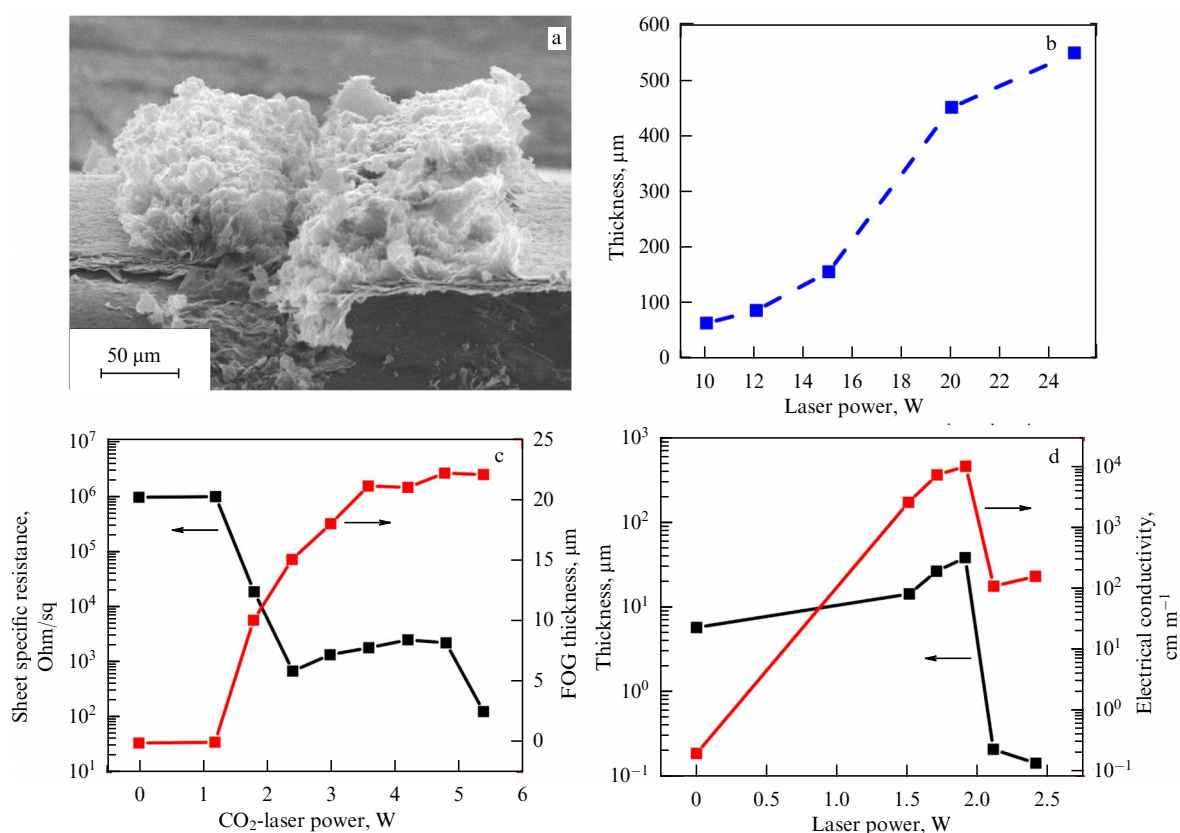
Figure 7. CO_2-laser impact on GO films. (a) Image of GO and RGO surface after laser annealing. (b) Increasing the film thickness (mainly due to porosity) with increasing laser power [76]. (c, d) Relationship of the thickness to electric characteristics and the threshold nature of the GO thermal expansion effect [77, 92].

(1) fast reduction of upper layers and screening of further penetration of radiation into the interior, absorption of the incident radiation, and heating of the upper layers up to ablation of the layer [88];

(2) gradual heating and reduction of the entire structure with an insignificant gradient over the film thickness; at the interface between the GO film and the substrate, the latter experiences no modifications and no composite is formed [99, 122];

(3) the GO structure is heated at high powers and is able to modify the substrate surface, including the formation of a composite with the chosen material [48, 123, 124];

(4) partial or complete ablation of the layer under high density of energy incident on the GO surface [110, 112].

4.4 Effect of substrate on graphene oxide reduction

In recent years, many papers have been published on l-RGO investigation, in which the authors compete with each other in how efficiently they managed to remove oxide groups from the surface of GO in a particular experimental setup, to restore the bonds between carbon atoms, and finally to obtain conductivity comparable to that of graphene [7, 29, 122, 125]. In these cases, the variation in substrates is not high: glass [88], silicon [126] and its oxides [92], PET [114, 127], and kapton (polyimide, PI) [128] are mainly used. Kapton is, however, more often used, not as a substrate for l-RGO, but as a precursor for direct synthesis of laser-induced graphene (LIG) under exposure of a polymer to laser radiation [129,
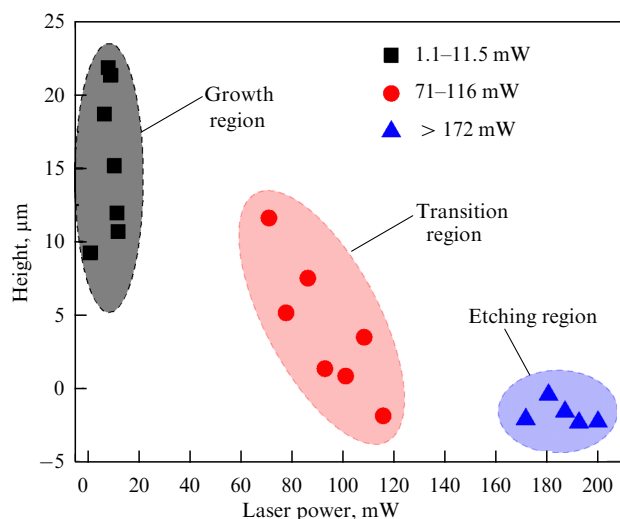
Figure 8. l-RGO thickness value under laser exposure with a wavelength of 650 nm and various values of power, as well as the conditional indication of growth, transition, and etching regions [112].

130]. In most papers, the authors do not note the dependence of the degree of reduction on the substrate used. For example, in Ref. [95], a photochemical and low-temperature reduction mechanism is suggested, which implies its compatibility with any substrate. At the same time, under photothermal action, it is necessary to take into account the effect of the interface between two media, the GO and the substrate material. Thus, in Ref. [48], it was shown that the addition of polystyrene balls into the GO matrix facilitates heat removal from graphene flakes and the formation of a composite material that prevents the burning of GO films. The use of a silicone material [124] and PET [114] as a surface for depositing and the subsequent reduction of GO has shown that the interface can experience changes (melt) because of strong GO heating [123].

Basically, researchers try to avoid such regimes and optimize the parameters of radiation sources to obtain a pure RGO film. For example, Ref. [122] proposed a technology of GO reduction on a PET substrate with subsequent transfer of the structure onto a flexible substrate of polydimethylsiloxane (PDMS).

It is also worth noting that the process of GO graphitization depends on the substrate material. This is confirmed by the fact that l-RGO on stainless steel (having high heat conduction) has a lower degree of graphitization [94]. However, it is difficult to assess quantitatively the substrate contribution based only on this experiment. In addition, a necessity arises to take into account the heat capacity, substrate optical properties, roughness, etc.

4.5 Electric conductivity of l-RGO

One of the popular and available indirect methods of evaluating the degree and quality of GO reduction is to measure the electric resistance of l-RGO structures, the sheet resistance of films, and the specific conductance of the material. However, the data are comparable only in the case of assessment of a GO conductance change upon laser processing in a given particular experiment. This is due both to the initial spread of GO conductance values (which vary from 10^{-4} to 10^1 S m^{-1} [66, 116, 118]), depending on the method and feedstock for the synthesis, and to differences among l-RGO structures (variations in thickness and poros-

ity, ablation, burning, change in atomic hybridization, etc.), considered above.

The electric resistance on average changes by 4–6 orders of magnitude with an increase in laser radiation power (see Figs 5 and 7). According to the data presented in Section 7, the l-RGO sheet resistance can vary from 2×10^5 to 10 Ω/sq. In addition, there is the influence of the scanning speed (degree of overlap) of the surface by the laser beam. The specific conductance of l-RGO changes in the range from 19 to 45.5 S m^{-1} when the speed varies from 0.1 to 5 μm s^{-1} [99].

4.6 Reduction of graphene oxide in suspensions

GO reduction in films is the most common approach. However, this option is not unique. One more solution, a less popular one, is the reduction of suspensions. For example, the exposure of a solution of graphite oxide in a quartz cuvette to an excimer ultraviolet laser with a wavelength of 248 nm was demonstrated. In this case, initially, the heating of a region near the cuvette edge occurs (to a temperature of 50–60 degrees), and then, due to the circulation of the solution from hotter to colder regions, the reduction of the entire solution is implemented, with the liquid changing its color from yellowish-brown to black. The authors of the sited paper propose as the main mechanism photochemical reduction based on the threshold proposed in the paper by Smirnov (3.2 eV). In this case, the energy of photons amounts to 5 eV and the intensity does not exceed 10^8 W cm^{-2}, which indirectly indicates the prevalence of a photochemical mechanism of reduction.

By exposing the matrix in which GO is located (in particular, water) to a laser, it is possible to initiate the radiolysis process with decay products capable of reducing the graphene oxide. There are two ways to activate this mechanism: by exciting water molecules by a femtosecond laser at a wavelength of 800 nm [125], or by a high-energy electron beam [53], which leads to the decay of H_2O (radiolysis) with the release of a hydrated electron, which is a strong reducer with respect to the oxygenic groups. Thus, the GO reduction may occur without significant heating or additional chemical reagents.

It should be noted that reduction in suspensions is technically more complex. In this case, the option is also lost to choose the size and the shape of the reduced areas; therefore, this method has not become widely used.

5. Application

The unique properties, environmentally friendly synthesis protocol, and the power to choose the modified region geometry make l-RGO an attractive material for electronics, energy transmission and storage, sensorics, and medical applications. To wit, the material has already been used in a number of devices (Fig. 9): power storage devices, various sensors, and the optoelectronic devices described in this Section. l-RGO has also been applied to modify surface properties, namely, to create superhydrophobic coatings [97] and membranes [132], and in photocatalysis [133, 134].

5.1 Supercapacitors

One of the advanced fields of l-RGO application is the creation of supercapacitors, devices combining the advantages of batteries (high energy density) and capacitors (high specific power). This allows high-efficiency accumulation, storage, and use of electric energy, which is particularly urgent for portable instrumentation, e.g., for fast charging smartphones [135]. The
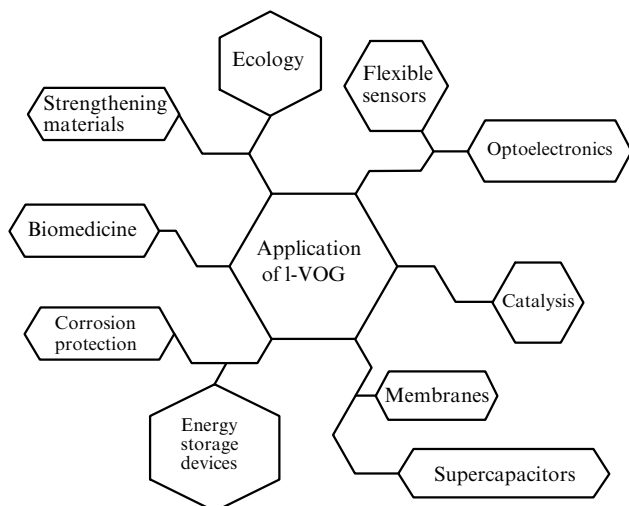
Figure 9. Trends in and areas of l-RGO application.

properties of carbon materials, including l-RGO, allow increasing the efficacy of conversion, storage, and power characteristics of energy carriers due to high conductivity, the large area of the electrically active surface, temperature stability, and corrosion resistance [136].

In the above sections, it was shown that, under the conditions of photothermal impact on GO, it is possible to obtain a highly porous material (Fig. 7a), which positively affects the characteristics of supercapacitors in general. For example, the application of l-RGO as a material for an electrode manufactured from GO suspensions reduced by an excimer laser has been demonstrated. The maximum specific capacitance value of 81 F g^{-1} was achieved under laser irradiation in the continuous-wave regime with an energy of 300 mJ for two hours. However, after an increase in the flux energy to 500 mJ, the capacitance decreased to 52 F g^{-1}, and to 59 F g^{-1} when the exposure time was reduced to 1 hour, keeping the energy equal to 300 mJ [131]. In turn, the GO reduced using a CO_2 laser on a PET substrate has shown a specific capacitance of 82 F g^{-1}. To increase the capacitance, MnO_2 nanoparticles were deposited on the conducting film. Such an approach is commonly used to make pseudocapacitors; in this case, the value of specific capacitance increased to 172 F g^{-1} [137].

A flexible electrochemical capacitor fabricated using Light-Scribe™ technology by irradiation of GO films in a DVD drive proved itself energy capacious [138]. The process is based on using grayscale gradation to regulate the laser beam power density, which allows obtaining different degrees of reduction in the graphene oxide film [122]. The resulting l-RGO film has a high specific conductance (1738 S m^{-1}) and stability (1% change in resistance for every 1000 bending cycles). The specific surface area in this case was 1520 $m^2\,g^{-1}$, the volt-ampere characteristic shape was close to theoretically perfect, and the value of specific capacitance amounted to 265 F g^{-1} in an organic electrolyte.

Using a combination of l-RGO with ferrocene nanocrystals that have a low oxidation potential can substantially improve the supercapacitor properties. For example, structures with a surface area of 720 $m^2\,g^{-1}$ and specific capacitance of 178 F g^{-1} were obtained (before ferrocene functionalization of 61 F g^{-1}) [139].

Moreover, the use of GO films with a thickness of a few micrometers or more allows making planar and 'sandwich' capacitors without using a substrate or electrolytes. The maximum specific capacitance amounted to 0.51 mF cm^{-2}

for a one-sided capacitor. In this case, the GO located between the etched l-RGO regions contains water and plays the role of a membrane ion separator [77].

Nevertheless, although the developed surface of carbon allotropes facilitates an increase in the electrode specific surface area and increases the capability of the device to accumulate charges, the currently available values are still far from the theoretical value for graphene (550 F g^{-1} with a specific area of 2675 $m^2\,g^{-1}$) [140], because the l-RGO structure inevitably remains defective.

5.2 Sensors and touch devices
l-RGO is significantly inferior to graphene in conductivity values, which is due to the presence of inhomogeneities, defects, and residual oxygen groups in its structure. However, exactly defects of this kind are adsorption centers, which makes the material sensitive to some molecular compounds and allows using it in the production of flexible biosensors, environment state sensors, and medical devices, as well as in the Internet of Things [141].

RGO-based sensors are successfully used to detect oxygen, carbon monoxide and dioxide, ammonia, and water vapor [6, 142]. The detection of nitrogen oxide with a sensitivity to 4 ppm at room temperature was demonstrated with a sensor response time of 10 s (the desorption–reduction time being 7 s), which is less than one third the values for unreduced GO [143]. The use of a DVD drive (laser wavelength 788 nm) to obtain l-RGO on a PET substrate with subsequent transfer onto a more flexible substrate of PDMS also allowed creating a sensor for detecting NO_2 in a concentration of 20 ppm (Fig. 10a) [122]. To improve the electric properties and to increase the electrically active area, platinum nanoparticles were uniformly deposited on the sensor surface.

The practice of surface functionalization with plasmonic nanoparticles or photosensitizers to improve sensitivity is widespread [144–146]. The application of both components leads to a synergetic combination of their properties. Thus, the nanostructures integrated *in situ* increase the effective surface area by several times and have high catalytic activity to some gases at room temperature. The analyte is catalyzed on the surface of noble metals and the electrons pass to the graphene electrode [142]. Using the same principle, a two-channel SPE-configured sensor was created for detecting organic compounds (the validation was carried out with the 4-nitrobenzenethiol molecule) by the methods of giant Raman scattering (GRS) and cyclic voltamperometry [128]. This sensor can also be used to detect other compounds, e.g., pesticides (Fig. 10b). Other l-RGO-based electrochemical sensors are applied to detect various compounds, e.g., hydroquinone and pyrocatechol [147], and GRS sensors are used to detect DNA [148].

l-RGO is also a material for manufacturing temperature sensors. The sensitive element made of GO placed between two glasses and exposed to CW laser radiation (wavelength 970 nm) exhibits a nonlinear dependence of the resistance on temperature in two ranges: from 303 to 353 K in air and from 80 to 300 K in a strong vacuum. It is interesting that the dependence of the temperature coefficient of electric resistance (TCR) is practically linear; this coefficient amounts to -8.09×10^{-3} K^{-1} at a temperature of 121.5 K and -5.12×10^{-3} K^{-1} at 299.2 K [149]. A temperature sensor based on l-RGO after irradiation by a laser with a wavelength of 550 nm has a perfectly linear (0.489% × K^{-1}) characteristic in the range of 243–308 K. A wireless readout of data allowed measuring the real variations in outdoor air temperature for a day [141].
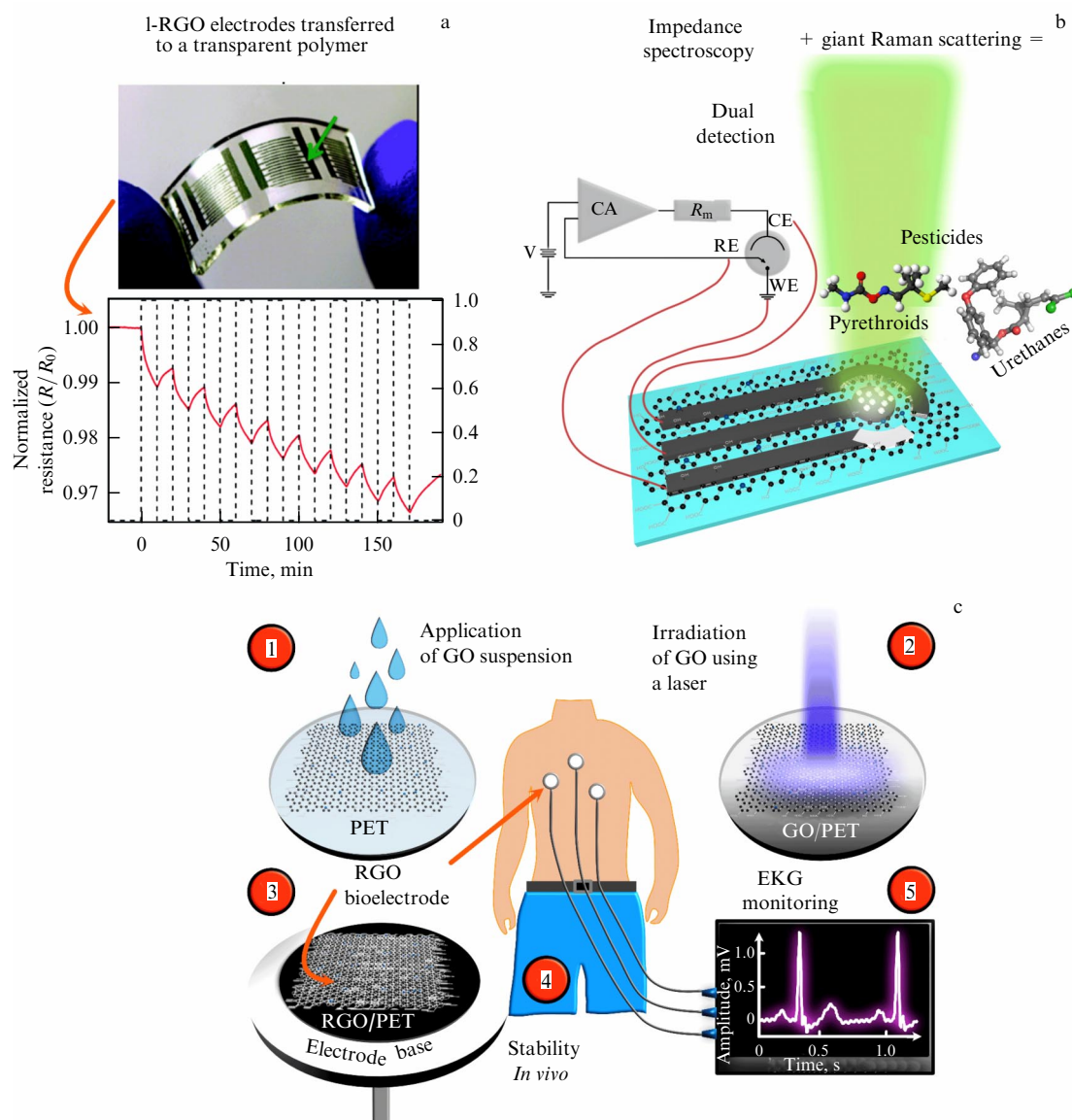
Figure 10. (a) Flexible rigged l-RGO electrodes and detection of NO₂ with a concentration of 20 ppm using them [122]. (b) Schematic image of a double-channel l-RGO sensor and its application for detecting pesticides by giant Raman scattering and impedance spectroscopy methods. (c) Schematic of the process of fabricating bioelectrodes of l-RGO for recording heart rhythm [123].

The change in the protonic and ionic conductance of GO under various conditions, including different levels of humidity, underlies the idea of 'electronic skin' — a combination of flexible and stretchable electronic sensors capable of imitating the function of human skin [150]. In this case, the GO itself was used as a sensitive layer and l-RGO as a conductor. This sensor demonstrates high sensitivity and fast response. Underclothes bioelectrodes made of l-RGO (irradiation of GO film with a diode laser at 405 nm) have shown unique properties of converting electric current of the first kind into human bioelectric currents and back without using additional, sometimes allergenic, gels. Moreover, the electrodes that were in contact with the skin for 108 hours are capable of ensuring an electrocardiogram record at an acceptable level (Fig. 10c) [123]. Standard Ag/AgCl electrodes fail after 24–48 hours because of gel degradation [151].

5.3 Electronic devices

GO's electric properties significantly change depending on the laser radiation parameters. This circumstance allows designing all-carbon semiconductor devices. Thus, based on an l-RGO, a field-effect transistor was fabricated within a single technological process: high intensity laser radiation was used to create electric conducting terminals (source, gate, and drain), and low intensity radiation, to form a semiconductor channel between them [152]. Moreover, the field-effect transistor, in which l-RGO serves as a material for the source and drain electrodes, retains its operability at a temperature of 200 °C (in a nitrogen atmosphere) for an hour [95].

Optimization of electric contacts and the laser impact on GO films allowed creating a memristor with a Q-factor of 11.9 (the ratio of resistance in the high-ohmic state, 896 kΩ, to that in the low-ohmic state, 75 kΩ). This result was achieved using a laser with a wavelength of 405 nm and a power of 70 mW [153]. The prototype volt-ampere characteristic presented in Fig. 11a takes the form of a hysteresis loop and has two switching potentials: near +2.5 V and −2 V. The pulsed memory state readout (0.2 V/50 ms) for 4 hours after the memristor recording shows the nonvolatility of the cells.
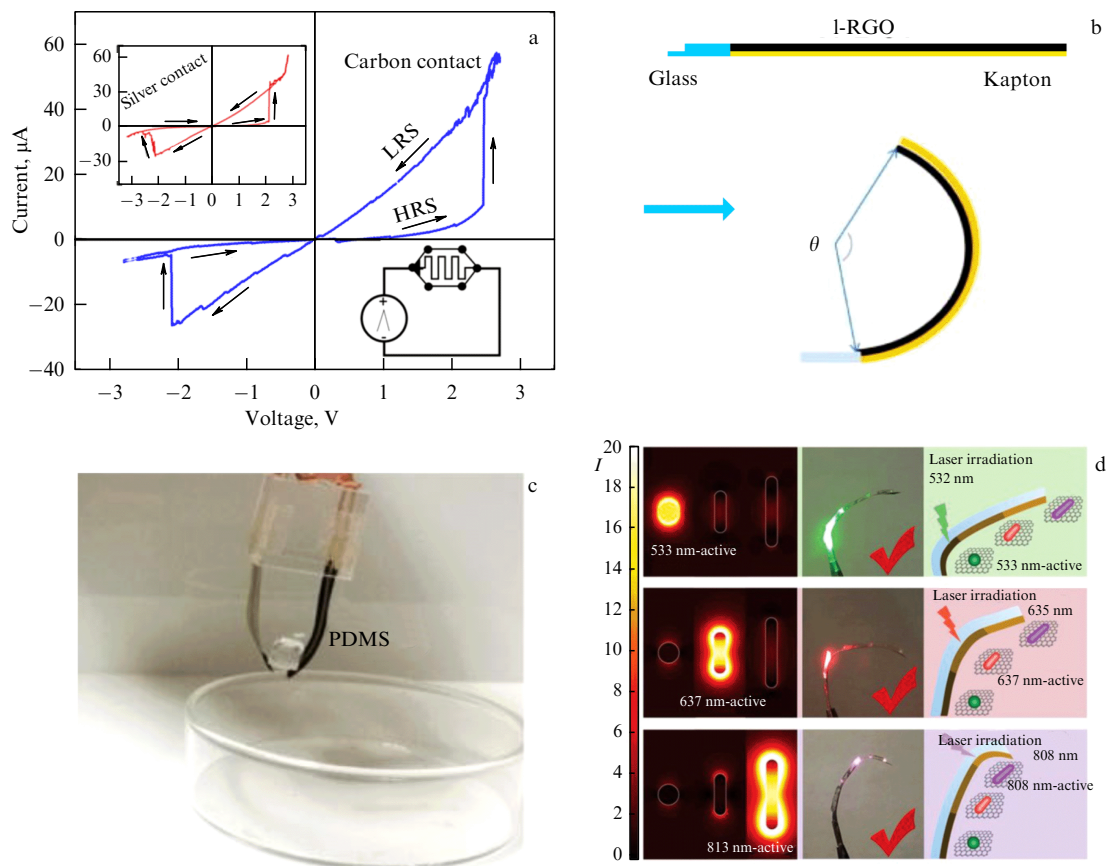
Figure 11. (a) Hysteresis loops of a memristor with different types of contacts [153]. (b) Schematic image of an actuator. (c) Prototype of a hand formed by two actuators in the process of moving a piece of PDMS [154]. (d) Computer models of electric field enhancement for silver nanorods of different sizes (with different wavelengths of the absorption maximum) with the corresponding response in the prototype [155].

In automated manufacturing, bionic hands with smooth motion control are increasingly in demand, especially when working with fragile objects. Operation units, elements, actuators, and drives serve to transform the input signal into mechanical movement. Table 2 presents examples of using l-RGO in thermoactuators, devices in which electric currents give rise to heating and, due to a high difference in thermal expansion coefficients, the shape and geometry of the movable part change. Thus, the appropriate movement occurs. For example, an l-RGO actuator on a flexible substrate of polyimide (PI) (Fig. 11b) can bend by an angle up to 270° at a voltage of 65 V [156]. At the same time, the addition of silver nanoparticles allows decreasing the voltage used by 50%; in this case, the bend angle amounts to 195°. The prototype of such a grip can successfully move a deformation-sensitive object (PDMS, Fig. 11b) over an obstacle.

Moreover, it is possible to control such executors by means of light. The concept of 'artificial muscles' that need no connecting 'joints' is based on a combination of l-RGO with golden nanorods of various shapes and sizes. Such an approach allows selective excitation of impurities, depending on the irradiation wavelength, which leads to various deformations of the actuator (Fig. 11d) [155]. Based on such microdrives, mini-robots were assembled — models of a human hand, flytrap plant, and eight-legged spider.

5.4 In optics
GO films can be used to fabricate thin planar lenses, based on the dependence of the refractive index and absorption

Table 2. Comparison of thermoelectric actuators [154].

Material	Response time, s	Bend angle, degrees	Supply voltage, V	Source
GO/l-RGO	—	68	35	[157]
l-RGO/PDMS	10	35.8	9	[158]
l-RGO/PI	8	270	65	[156]
l-RGO/Ag nanoparticles/PI	6	195	28	[154]

coefficient on the degree of material reduction. The lens is formed by the alternation of concentric l-RGO and GO circles [74, 159]. This lens operates according to the principle of 3D focusing of the transmitted interfering beams and is descried by the Rayleigh–Sommerfeld diffraction theory (Fig. 12a) [160].

A similar approach was applied to fabricate a polarizer from a thin GO film. The periodic structure of C-shaped elements operates in the range from 600 nm to 1.6 μm according to the waveguide principle (as in photonic crystals) [161]. Figure 12b shows the dependence of the transmission coefficient for waves with different polarizations (TE and TM) on the light wavelength. Moreover, fast and precise scanning of the laser beam allows creating light-emitting diode structures of various shapes and sizes. For example, an l-RGO playing the role of the bottom electrode was fabricated in the form of a ladder and a bow (Fig. 12c) [162].

Figure 12. (a) Schematic image of changes experienced by a wavefront when passing through a lens; inset shows the lens optical profile (scale of 2 μm) [161]. (b) Transmission spectrum of a polarizer for longitudinal and transverse light pola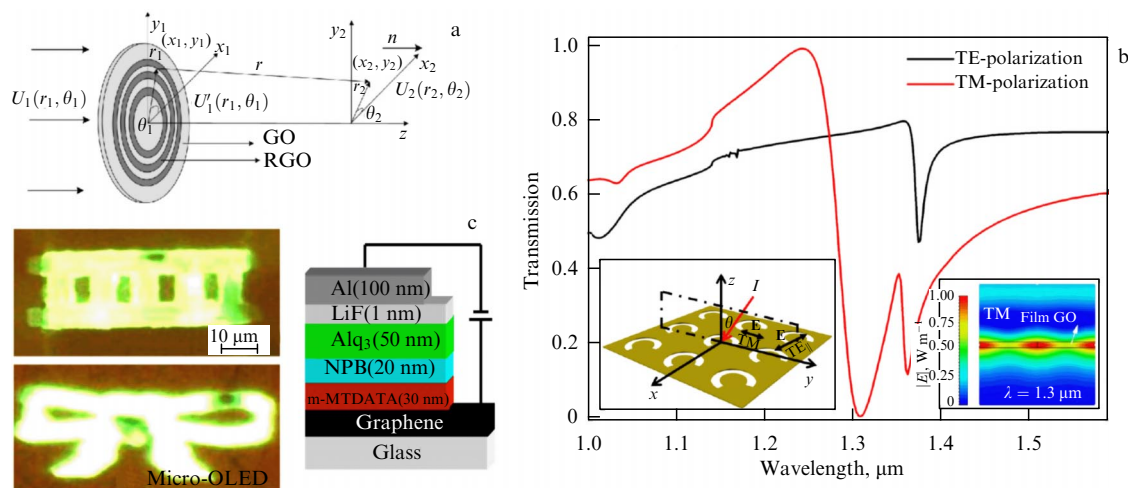rization; left inset shows the design of the C- shaped polarizer, right-hand inset illustrates computer simulation of trapping incident light with transverse polarization [161]. (c) Organic light-emitting diodes with various configurations of l-RGO electrodes and schematic representation of their structure [162].

The reduced GO possesses photocatalytic properties. So, to improve the switching characteristics of a photoresistor, a copper oxide + RGO nanocomposite was used. The switching (response) time was 0.45 s, and the ratio of states was 3.25 under exposure to 20 mW, 532 nm for the fabricated prototype [163].

In the above sections, the temperature dependence of l-RGO resistance was considered. In addition, l-RGO has a high absorption coefficient, which is used to design bolometers. In this type of device, it is important for the material to have a minimum reflection coefficient and a high efficiency of converting the incident radiation into heat. In one of the publications [101], the maximum absorption amounted to 98% for a film a few micrometers thick. The measurements were performed by means of light from an incandescent lamp focused with a lens to a power density of 216 mW cm^{-2} at a constant voltage of 0.5 V. The radiation hitting the bolometer caused a change in the current value within 0.4%.

6. Conclusion and prospects for development

Carbon has more than 500 allotropes, most possessing unique physical and chemical properties, which allows using them in many fields of production. One of the promising areas is the transition to all-carbon electronics, which is cheaper, more environmentally friendly, more energy efficient, and more compact than the silicon variant [122, 164].

In this paper, we present a review of one such carbon material, graphene oxide (GO), reduced by laser radiation. The GO properties radically change with the removal of oxygenic groups and water molecules, as well as under a change in the electronic configuration of atoms in a monoatomic layer (graphene). This article is of interest both to novices who are just beginning to get acquainted with GO and its modifications and to experienced researchers in order to systematize information. The paper considers fundamental properties of the material, as well as its application in new energy efficient devices, facilitating the formulation of new research tasks and the solution to already established ones.

In the paper, attention is focused on photoinduced processes that occur under exposure of GO films to laser radiation. Thus, we consider the mechanisms of GO conversion into l-RGO, the degree of material reduction, the influence of radiation source parameters on the l-RGO structure, conductance, porosity, and thickness of the obtained films. Threshold phenomena, such as burning, saturation, and ablation, are also assessed. Based on the available literature data, a summarizing table is presented (Table 3, according to our data, is the most complete comparative work on the GO laser annealing method; see Appendix).

However, the creation of a nonlinear model of reduction to predict l-RGO structures with specified properties as well as substrate influence in the process of laser GO annealing are only a few of the issues researchers are facing. For example, this data could facilitate the efficient production of electronic circuits from a single material in a single process, which would significantly reduce the production load and cost of electronics production. One more open question is the use of the material as a sensor. For example, biomedical properties of l-RGO and the possibility of its application in flexible portable sensors require further investigation.

Already now, the reduction of graphene oxide is a promising way to produce graphene (at present, unfortunately, containing many defects) in large quantities. l-RGO structures find wide application in many fields of modern electronics and material science, from energy storage to sensors used in environmental monitoring, and actuators in robotics.

7. Appendix

Our review article is based on data from GO photoreduction studies depending on the irradiation sources, duration of pulses, frequency, and other features of processing and sample preparation. Therefore, the basic parameters affecting the reduction of GO films were systemized in a summary table. Unfortunately, the data presented in the literature are often incomplete, resulting in some cells being left blank.

Table 3. Results of research work on laser irradiation of GO under various conditions.

Radiation source parameters								Additional factors affecting GO reduction		
Wave-length, nm	Pulse duration, s	Pulse repetition rate, Hz	Beam energy, J	Power, W	Energy density, mJ cm⁻²	Power density, W cm⁻²	Surface scanning speed, mm s⁻¹	Substrate material	External environmental conditions, special conditions of sample preparation	GO film thickness
46.9	1.5×10^{-9}	—	1.5×10^{-4}	—	to 800	—	—	Al_2O_3/Si (100)	—	—
248	5.0×10^{-9}	500	—	—	48–240	—	—	PET	20 degrees, s.c., 30% humidity. Overlap coefficient ranges from 2 to 50	20–25 μm
248	2.0×10^{-8}	1	—	—	60–190	—	0.2	Glass	Square beam 10 by 10 μm, pre-irradiation with one pulse 65–75 mJ cm⁻²	40 nm
248	—	10	0.3–0.53	—	—	—	—	Irradiation in solution followed by deposition of the suspension onto silicon	Graphite oxide, irradiation time 1–2 hours	—
248	20×10^{-9}	5	200×10^{-3}	—	—	—	—	Aluminum foil	—	—
248	2.5×10^{-8}	1	—	—	60–400	—	—	GO film without substrate	Graphite oxide, reduction in three modes: in a high vacuum ($\sim 10^{-6}$ Torr), in a low vacuum (9.8×10^{-2} Torr), and in a nitrogen flow from 2 to 32 pulses. Drying the GO sample at a temperature of 105°C for 24 hours	5–8 μm
248	2.0×10^{-8}	1	—	—	80	—	—	PET, silicon oxide, titanium, and gold electrode structure	In helium at 100 Torr. Number of pulses from 10 to 1200	—
248	2.0×10^{-8}	10	—	—	6–12	—	—	GO film without substrate	6000 pulses	—
266	6.0×10^{-9}	30	—	—	50	—	1	Silicon plate	s.c., one region irradiated 5 times	—
308	2.0×10^{-8}	100	0.105	5.0×10^6	—	—	—	GO film without substrate	—	—

	Assessment of l-RGO Raman spectra					X-ray photoelectron spectroscopy (XPS) of l-RGO structures [* — our calculation]	l-RGO resistance or conductance	Application	Reference
Wavelength, nm	Peak D halfwidth/ (peak position), cm^{-1}	Peak G halfwidth/ (peak position), cm^{-1}	Peak 2D halfwidth/ (peak position), cm^{-1}	Ratio I_D/I_G [* — our calculation]	Ratio I_{2D}/I_G				
633	—	—	—	1.35 (GO) 1.31 (200 mJ cm^{-2}) 1.40–1.375 (graphically)	—	—	—	Nanoelectronics	[47]
532	—/($\sim$ 1350)	—/($\sim$ 1580)	—/($\sim$ 2700)	$\sim$ 0.96–1.17	$\sim$ 0–0.55	1.09 C–O/[C = O+ +C(= O)O] 10.84 C/O (0.12 J cm^{-2} 40 pulses)	—	—	[94]
514	—/($\sim$ 1351– 1344)	—/($\sim$ 1590– 1569)	64/($\sim$ 2700)	*0.56	—	—	2.5 kΩ 75 mJ cm^{-2} 1 kΩ 100 mJ cm^{-2} 7.9 kΩ 190 mJ cm^{-2}	Nanoelectronics	[113]
—	—	—	—	—	—	3.2 CC/CO 61% (C = C)	—	Supercapacitors	[131]
632.8	—/(1336)	—/(1586)	—	1.03 before irradiation, 1.08 after	—	8% C–O 7.6% C = O	53.8 kΩ/sq	Composite material	[165]
532	—/($\sim$ 1342) 32 pulses, 138 mJ cm^{-2}	—/($\sim$ 1575) 32 pulses, 138 mJ cm^{-2}	Peak G′, 50–65/(2672) 32 pulses, 138 mJ cm^{-2}	—	0.1–0.5 $I_{G'}/I_G$, high vacuum 0.1–0.4 $I_{G'}/I_G$, in nitrogen	10–40 C/O high vacuum 10–40 C/O in nitrogen	491 Ω/sq 204 mJ cm^{-2} in low vacuum up to 130 pulses	Nanoelectronics	[120]
473	75–85/(1354)	75–56/(1595)	—/(2695)	0.79–1.0	—	16% of oxygen-bound carbon, 120 pulses	—	Transistors	[95]
532	—	—	—	0.86–0.92	—	3.7–6.9 C/O (determined by RBS and ERDA methods)	Current-voltage curves from flow	Micro- and photo-electronics	[166]
532	117/(1351)	70/(1579)	145/(2679)	1.22	0.21	79 C/O	—	—	[167]
—	—	—	—	—	—	—	—	Supercapacitors	[168]

Table 3 (continued)

Radiation source parameters								Additional factors affecting GO reduction		
Wave-length, nm	Pulse duration, s	Pulse repetition rate, Hz	Beam energy, J	Power, W	Energy density, mJ cm^{-2}	Power density, W cm^{-2}	Surface scanning speed, mm s^{-1}	Substrate material	External environmental conditions, special conditions of sample preparation	GO film thickness
355	1.5×10^{-8}	5	—	—	40–85	—	—	Flexible polyimide film from Kodak	RGO films printed on a printer, s.c., each point was irradiated for 20 s, spot size ~ 0.28 cm^2	3.5 µm for 60 layers
355	—	10^5	—	—	0.153–0.525	—	50	Powders in a quartz tube	Beam size 5 mm, number of irradiation cycles 10, pulse overlap 99.9%, distance between lines 20 µm	—
355	1.0×10^{-8}	10	—	0.4	—	—	—	Glass plate	Double-beam interference of a laser beam. Period of patterns from 1 to 4 µm	—
355	—	—	—	—	—	—	—	Silicon structured lattice plate	Double-beam interference of a laser beam. Beam size 8 mm in diameter before splitting	—
355	6.0×10^{-9}	30	—	—	85	—	1	Silicon plate	s.c., one area irradiated 5 times	—
405	—	—	—	0.015–0.300	—	—	3 min cm^{-2}	Kapton with GO, polyimide film	—	—
405	—	—	—	0.25	—	—	16.67	Silicone film	Etching carried out at 60% of laser power	—
405	—	—	—	0.015–0.300	—	—	—	Kapton	—	—
405	—	—	—	0.01–0.300	—	—	3 min cm^{-2}	PET	—	—
405	CW	—	—	—	—	—	5	PET film for laser printer	TiO$_2$ colloidal solution added	—

	Assessment of l-RGO Raman spectra					X-ray photoelectron spectroscopy (XPS) of l-RGO structures [* — our calculation]	l-RGO resistance or conductance	Application	Reference
Wavelength, nm	Peak D halfwidth/ (peak position), cm^{-1}	Peak G halfwidth/ (peak position), cm^{-1}	Peak 2D halfwidth/ (peak position), cm^{-1}	Ratio I$_D$/I$_G$ [* — our calculation]	Ratio I$_{2D}$/I$_G$				
532	—	—	—	—	—	—	$\sim$ 11–1.4 kΩ/sq 60 layers $\sim$ 7.5–1.7 kΩ/sq 50 layers $\sim$ 7.0–1.8 kΩ/sq 40 layers $\sim$ 30–1.9 kΩ/sq 30 layers $\sim$ 70–3.0 kΩ/sq 20 layers	Electrochemical devices	[169]
532	—	—	—	0.874–1.23	0.05–0.569	0.722–1.86 C/O	$\sim$ 1–80 MΩ	Mass production of graphene powders	[79]
514	—	—	—	—	—	10.2 C/O in X direction of the lattice 17.1 C/O in X and Y directions of the lattice	—	Superhydrophobic surfaces/holograms	[75]
—	—	—	—	—	—	6.8% oxide atoms	—	Superhydrophobic surfaces	[97]
532	112/(1349)	76/(1575)	132/(2683)	1.44	0.43	56.47 C/O	—	—	[167]
532	—	—	—	$\sim$ 1 (LIG)	—	—	$\sim$ 500–250 Ω/sq (LIG, 65–100 mW) $\sim$ 6 × 10^7–250 Ω/sq (l-RGO, 65–100 mW)	Capacitors	[170]
—	—	—	—	—	—	—	7.2 kΩ/sq	High voltage drives	[124]
532	—	—	—	$\sim$ 1 (LIG) up to 100 mV	—	* $\sim$ 8.5–9.9 50–100 mW	$\sim$ 500–250 Ω/sq (LIG, 65–100 mW)	Flexible Electronics	[130]
532	—	—	—	—	—	* $\sim$ 2.77 100 mW	$\sim$ 6 × 10^7–220 Ω/sq (65–105 mW)	Memristors	[153]
532	—	—	—	—	—	88.02% carbon, 9.51% oxygen, 0.51% nitrogen, 15.02% titanium	—	Electrodes and sensors	[171]

Table 3 (continued)

	Radiation source parameters							Additional factors affecting GO reduction		
Wave-length, nm	Pulse duration, s	Pulse repetition rate, Hz	Beam energy, J	Power, W	Energy density, mJ cm^{-2}	Power density, W cm^{-2}	Surface scanning speed, mm s^{-1}	Substrate material	External environmental conditions, special conditions of sample preparation	GO film thick-ness
445	1.05×10^{-6}–2.14×10^{-6}	—	—	10.23×10^{-3}–40×10^{-3}	15.2–59.4	—	1.5	PET	Air pumped through chamber	39–65 nm
488	—	—	—	to 10.5×10^{-3}	—	—	—	Silicon plate SiO$_x$	Exposure 10 times for 10 s	—
514.5	—	—	—	to 7×10^{-3}	—	—	—	Silicon plate SiO$_x$	Exposure 10 times for 10 s	—
515	2.8×10^{-13}	5.0×10^5	7.0×10^{-6}–60×10^{-6}	—	—	—	5–100	PET	—	0.5 µm
532	2.0×10^{-1}	—	—	0.1×10^{-3}–10×10^{-3}	—	7.5×10^7–7.53×10^9	—	Glass coated with gold film	Air, beam diameter 1.3 mm	103 nm
532	—	—	—	0.012	—	—	0.05	SiO$_2$/Si	—	32 nm
532	5.0×10^{-9}	10	0.3	0.3	—	—	—	GO suspension	Exposure time 3, 5, 7, or 10 minutes. Unfocused 7-mm beam diameter	12 nm
532	7.0×10^{-9}	30	0.03–0.08	—	100	—	—	Flexible GO film without substrate	Exposure time 6–180 s (without focusing, quantum energy 2.32 eV)	55 µm

	Assessment of l-RGO Raman spectra					X-ray photoelectron spectroscopy (XPS) of l-RGO structures [* — our calculation]	l-RGO resistance or conductance	Application	Reference
Wavelength, nm	Peak D halfwidth/ (peak position), cm^{-1}	Peak G halfwidth/ (peak position), cm^{-1}	Peak 2D halfwidth/ (peak position), cm^{-1}	Ratio I_D/I_G [* — our calculation]	Ratio I_{2D}/I_G				
—	—	—	—	—	—	—	4,16– 0.603 kΩ	Biosensors	[172]
488 514.5 632.8	$-$/($\sim$ 1359– 1353) for films $-$/($\sim$ 1354– 1348) for flakes	—	—	$\sim$ 1.8–2.4 for films $\sim$ 2.2–2.9 for flakes	—	—	—	Nanoelectronics	[98]
488 514.5 632.8	$-$/($\sim$ 1354– 1349) for films $-$/($\sim$ 1350– 1345) for flakes	—	—	$\sim$ 1.4–2.15 for films $\sim$ 2.45–3.4 for flakes	—	$\sim$ 18 C/O 0.77 mW, 600 s	—	Nanoelectronics	[98]
532	—	—	—	0.78–1.04 depending on speed and energy of the beam	0.1–0.4 depending on speed and energy of the beam	1.36 C/O 15 nJ, 50 mm s^{-1}	0.2– 1.2 kΩ/sq 15–60 nJ, 10– 50 mm s^{-1}	Biosensors, flexible bolometers, radio emission sensors	[114]
532	140–180/($-$)	—	—	1.026–0.995	0.18–0.4 of the ratio of second-order peak areas to D peak area	—	10^{11}–10^5 Ω	—	[121]
532	—	—	—	0.96	—	3.7% (C=O)	$\sim$ 16 S cm^{-1} 30–60 μS 6 mW, number of exposures 2–7	—	[118]
785	—	—	$-$/($\sim$ 2679)	1.3 10 min	0.025 10 min	21% (O/C) 10 min	4.4 × 10^5 Ω/sq	Production of l-RGO suspensions	[66]
—	$-$/(1347) 30 mJ, 10 s	$-$/(1594) 30 mJ, 10 s	$-$/(2681) 30 mJ, 10 s	—	—	7.43 C/O 50 mJ, 60 s	$\sim$ 0.8 × 10^{-5}– 0.9 × 10^{-3} S cm^{-1} 30 mJ, up to 3 min $\sim$ 0.9 × 10^{-5}– 0.9 × 10^{-3} S cm^{-1} 50 mJ, up to 3 min $\sim$ 0.15 × 10^{-3} –0.8 × 10^{-3} S cm^{-1} 80 mJ, 6 s. Frequency range in which resistance was measured: 10 × 10^2– 10 × 10^6 Hz	NH$_3$ gas sensors	[173]

Table 3 (continued)

	Radiation source parameters							Additional factors affecting GO reduction		
Wave-length, nm	Pulse duration, s	Pulse repetition rate, Hz	Beam energy, J	Power, W	Energy density, mJ cm^{-2}	Power density, W cm^{-2}	Surface scanning speed, mm s^{-1}	Substrate material	External environmental conditions, special conditions of sample preparation	GO film thickness
532	6.0×10^{-9}	30	—	—	150	—	1	Silicon plate	s.c., one area irradiated 5 times	—
632.8	—	—	—	to 4.5×10^{-3}	—	—	—	Silicon plate SiO$_x$	Exposure time 10 times for 10 s	—
663	CW	—	—	0.08	—	3.4×10^5	1.5×10^{-2}	Quartz plate with GO + PEI film layer by layer	Nitrogen, beam diameter ~ 3 μm	—
780	7.0×10^{-14}	5.0×10^7	—	0.003–0.013	—	—	5.0×10^{-3}–0.1×10^{-3}	Glass plate	n.s., diameter 2 μm	110 nm
780	—	—	—	—	—	—	—	Polyester film	—	—
788	CW	—	—	—	—	—	—	PET	20 degrees, air, 30% humidity, 6 passes per etching	20–25 μm
788	—	—	—	0.005	—	—	—	PET	—	—
790	1.2×10^{-13}	8.0×10^7	—	to 3.5×10^{-3}	—	—	—	Glass plate	600 μs for each point, step 100 nm	55 nm
800	1.0×10^{-13}	10^3	—	—	47–968	—	—	PET	20 degrees, s.c., humidity 30%, 40 pulses	20–25 μm
800	1.0×10^{-13}	300	—	—	10–140	—	—	—	Reduction time 60–180 min at distance of 35 cm (lens with a focal length of 50 cm)	aqueous suspension
800	10^{-13}	10^3	—	—	—	—	—	Cover glass	Polyvinyl alcohol mixed with graphene oxide. Beam size 0.55 μm at focus	—
800	—	10^4	—	—	—	—	—	PDMS	—	—
800	1.2×10^{-13}	8.0×10^7	—	—	—	—	—	Glass	—	—

Assessment of l-RGO Raman spectra						X-ray photoelectron spectroscopy (XPS) of l-RGO structures [*—our calculation]	l-RGO resistance or conductance	Application	Reference
Wavelength, nm	Peak D halfwidth/(peak position), cm^{-1}	Peak G halfwidth/(peak position), cm^{-1}	Peak 2D halfwidth/(peak position), cm^{-1}	Ratio I_D/I_G [*—our calculation]	Ratio I_{2D}/I_G				
532	100/(1347)	61/(1576)	118/(2678)	1.22	0.32	10.01 C/O	—	—	[167]
488 514.5 632.8	−/(∼ 1337–1333) for films −/(∼ 1339–1331) for flakes	—	—	∼ 1.9–3.1 for films ∼ 2.5–4.0 for flakes	—		—	Nanoelectronics	[98]
532	−/(∼ 1348)	−/(∼ 1566)	—	—	—	—	1.1×10^{-2} S cm^{-1}	—	[88]
514	—	—	—	1.11–1.41 1.13–1.37 relative to the range 0–65 mJ µm^{-2}	—	2.46–3.35 C/O 5 µm s^{-1} 1.02–1.76 (CC/CO)	19.0–45.5 5 mW, 1.25–25 mJ µm^{-2}	—	[99]
—	—	—	—	—	—	—	—	Biosensors	[174]
532	—	—	—	1.3	0.17	1.15 C–O/ [C=O+C(=O)O] 6 passes, maximum contrast in the program	—	—	[94]
514	—	—	—	—	—	27.8 C/O	2.0×10^{5}– 0.5×10^{2} Ω/sq, grayscale 1–5, repetitions 1–3	Batteries, sensors and electro-catalysis	[122]
514.5	—	—	—	0.89	—	∼ 61% carbon not bound with oxygen	9.09×10^{2}– 2.56×10^{4} Ω/sq 1–3 mW	Microelectronics	[7]
532	—	—	—	1.1	0.1	2.63 C–O/ [C=O+C(=O)O] 150 mJ cm^{-1}, 40 pulses	—	—	[94]
—	—	—	—	0.76–0.97 20– 80 mJ sm^{-2}, 60–180 min	—	7.4 80 mJ sm^{-2}	250.9– 3.3 Ω sm^{-1} 40– 80 mJ sm^{-2}, 60–120 min	Composite materials	[125]
—	−/(1348)	−/(1578)	−/(2688)	—	—	54% C–C/(C=C)	—	Holograms	[78]
—	—	—	—	—	—	—	—	Photonics and optoelectronics	[161]
514.5	−/(1354)	−/(1599)	—	0.89	—	72% carbon not bound with oxygen	7.68×10^{4}– 6.49×10^{5} Ω for the geometry considered in the paper	Graphene electronics	[111]

Table 3 (continued)

			Radiation source parameters						Additional factors affecting GO reduction	
Wave-length, nm	Pulse duration, s	Pulse repetition rate, Hz	Beam energy, J	Power, W	Energy density, mJ cm^{-2}	Power density, W cm^{-2}	Surface scanning speed, mm s^{-1}	Substrate material	External environmental conditions, special conditions of sample preparation	GO film thickness
1030	2.8×10^{-13}	2.0×10^{6}	—	to 20	5.6–56	—	—	Silicon plate SiO$_2$	Argon (10 l min^{-1}), $10^2 - 2 \times 10^4$ pulses per µm	23.5 nm
1064	2.0×10^{-8}	10^{4}	—	—	400– 2.8×10^{4}	—	—	Glass and silicon	Gaussian beam, 50 µm diameter. Overlap factor is 3	5–30 µm
1064	10^{-11}	10^{5}	—	—	100–400	—	10–100	OG film without backing	Liquid nitrogen, nitrogen (gas)	20–30 µm
1064	3.0×10^{-9}	—	0.05–0.2	—	—	—	—	—	Unfocused laser beam with an area of 1 cm^2	7 µm
1064	10^{-11}	10^{5}	7.0×10^{-8}– 5.0×10^{-7}	0.007– 0.05	48–320	—	5–100	Polycarbonate membrane filter	Dye (Congo Red), mixed with graphene oxide, beam with a diameter of 20 µm	1.2 µm
1064	—	5.0×10^{3}	—	—	150	—	—	PET	—	90 nm
1064	6.0×10^{-9}	30	—	—	380	—	1	Silicon plate	n.u., one area irradiated 5 times	—
1064	4.0×10^{-9}– 200×10^{-9}	1.6×10^{3}– 1.0×10^{6}	—	—	10^2–10^5	—	to 1.5×10^4	Silicon plate, glass	s.c., spatial resolution 20 lines mm^{-1}. Overlap coefficient ranges from 1 to 800	5 µm
1064	50×10^{-9}	90×10^{3}	—	—	—	10^6, 5×10^6, 10^7	500	Printed circuit board with aluminum electrodes, glass	—	—
9.3×10^{3}	—	—	—	4.8	—	—	—	OG film without backing	—	10–20 µm
10.6×10^{3}	—	10^{3}	—	10–25	—	—	200	GO film without substrate	In a nitrogen flow, size of Gaussian beam profile 3.9×0.23 mm^{-2}	16–18 µm
10.6×10^{3}	1.4×10^{-5}	—	—	to 5.4	—	—	—	Polyimide	—	—
10.6×10^{3}	—	—	—	1.5–2.4	—	—	—	Silicon plate	—	6 µm
10.6×10^{3}	—	—	—	1.2–5.5	—	—	—	GO film without substrate	—	22 µm

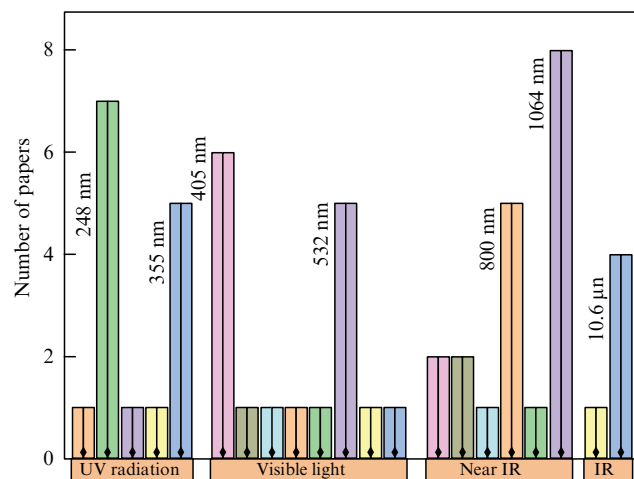| Assessment of l-RGO Raman spectra						X-ray photoelectron spectroscopy (XPS) of l-RGO structures [* — our calculation]	l-RGO resistance or conductance	Application	Reference
Wavelength, nm	Peak D halfwidth/ (peak position), cm^{-1}	Peak G halfwidth/ (peak position), cm^{-1}	Peak 2D halfwidth/ (peak position), cm^{-1}	Ratio I_D/I_G [* — our calculation]	Ratio I_{2D}/I_G				
532	—	—	—	—	0.25–0.8 9–56 mJ sm^{-2}	—	0.86–2.80 kΩ/sq 11–34 mJ sm^{-2}	—	[115]
—	—	—	—	0.97 (GO) ∼ 0.82 (l-RGO)	—	*4.5–5.54 (C–C/C–O) 4–28 J sm^{-2}	—	Bolometer	[101]
532	54/(1358) in nitrogen (gas) 46/(1355) liquid nitrogen	42/(1585) in nitrogen (gas) 34/(1578) liquid nitrogen	72/(2718) in nitrogen (gas) 67/(2708) liquid nitrogen	0.43 in nitrogen (gas) 0.2 liquid nitrogen	—	9.1 C/O in nitrogen (gas) 10.3 C/O liquid nitrogen	20 MΩ/sq (GO) 10^4 Ω/sq in nitrogen (gas) 50–60 Ω/sq in liquid nitrogen	Flexible and biocompatible electronics	[116]
—	—	—	—	—	—	7.55 C/O ion scattering spectroscopy, 36.9% (C–C), 20.9% (C–O) 200 mJ sm^{-2}	—	—	[175]
632.8	60–180/ (1331–1338)	48–100/ (1585–1592)	70–160/ (∼ 2656)	—	—	—	—	—	[89]
514	—	—	64 cm^{-1}/ (∼ 2691 cm^{-1})	* 0.594	—	0.09 O/C	1.07 × 10^{-4} Ω (500 Ω/sq)	Biomedical chips	[176]
532	95 cm^{-1}/ (1358 cm^{-1})	57 cm^{-1}/ (1578 cm^{-1})	247 cm^{-1}/ (2711 cm^{-1})	1.04	0.25	25.66 C/O	—	—	[167]
532	—	—	—	0.97–4.59	0–0.96	* 27.23 C/O	1000–60 Ω/sq	Gas sensor	[90]
532	—	—	—	1.2 (GO), 1.0 (l-RGO)	—	—	1.6 × 10^{-5} Ω m	Microelectronics	[110]
—	—	—	—	—	—	∼ 10.1 : 1 C/O	∼ 880 Ω/sq	Lithium-ion batteries	[119]
514 785	—	—	—	0.87–0.9 (26.5 W, 200 mm s^{-1}, 200 Hz, 0.5 ms pulse) 1.24–1.34	—	C/O 9.93 (26.5 W, 200 mm s^{-1}) 7.75 (18.6 W, 200 mm s^{-1}) 26.7 (26.5 W, 100 mm s^{-1})	0.22–5.5 Ω cm	Supercapacitors	[76]
—	—	—	—	—	—	—	15−35 Ω/sq (LIG)	Micro-supercapacitors	[129]
—	—	—	—	2.72 (1.9 W)	—	—	100−1000 S m^{-1}	Supercapacitors and solar panels	[92]
514.5	—	—	—	—	—	less than 20% oxygen 2.4 W, scanning speed — 30%	10^6 − 10^2 Ω/sq	Supercapacitors	[72]

Figure 13. Segmentation of publications by wavelength of laser sources. Largest number of studies on laser reduction of GO has been carried out at wavelengths of 248, 405, and 1064 nm. Sampling corresponds to the summary table above.

However, we hope that our readers will take into account these drawbacks when preparing subsequent publications, which will make the analysis of fundamental processes occurring in the photoreduction of GO and processing other materials more complete.

References

1. Ferrari A C et al. *Nanoscale* **7** 4598 (2015)
2. Novoselov K S et al. *Science* **306** 666 (2004)
3. Gubin S P, Tkachev S V *Radioelektron. Nanosist. Inform. Tekhnol. RENSIT* **2** (1–2) 99 (2010)
4. Jiat L X et al. *J. Taiwan Inst. Chem. Eng.* **98** 163 (2019)
5. Mishra N et al. *Phys. Status Solidi A* **213** 2277 (2016)
6. Tarcan R et al. *J. Mater. Chem. C* **8** 1198 (2020)
7. Zhang Y et al. *Nano Today* **5** (1) 15 (2010)
8. Wan Z et al. *Adv. Mater. Technol.* **3** 1700315 (2018)
9. Ye R, James D K, Tour J M *Adv. Mater.* **31** 1803621 (2019)
10. Kumar R et al. *Coord. Chem. Rev.* **342** 34 (2017)
11. Chernozatonskii L A, Sorokin P B, Artukh A A *Russ. Chem. Rev.* **83** 251 (2014); *Usp. Khim.* **83** 251 (2014)
12. Wallace P R *Phys. Rev.* **71** 622 (1947)
13. Pérez E M, Martín N *Chem. Soc. Rev.* **44** 6425 (2015)
14. Lonkar S P, Deshmukh Y S, Abdala A A *Nano Res.* **8** 1039 (2015)
15. Shulga Yu M, Shulga N Yu, Parkhomenko Yu N *Izv. Vyssh. Uchebn. Zaved. Mater. Elektron. Tekh.* (3) 157 (2014)
16. Poh H L et al. *Nanoscale* **4** 3515 (2012)
17. Paredes J I et al. *Langmuir* **24** 10560 (2008)
18. Yan J-A, Chou M Y *Phys. Rev. B* **82** 125403 (2010)
19. Brodie B *Ann. Chim. Phys.* **45** 351 (1855)
20. Staudenmaier L *Berichte Deutschen Chem. Gesellschaft* **31** (1898)
21. Hummers W S, Offeman R E *J. Am. Chem. Soc.* **80** 1339 (1958)
22. Marcano D C et al. *ACS Nano* **4** 4806 (2010)
23. Chen J et al. *Carbon* **64** 225 (2013)
24. Guerrero-Contreras J, Caballero-Briones F *Mater. Chem. Phys.* **153** 209 (2015)
25. Sheshmani S, Fashapoyeh M A *Acta Chim. Slov.* **60** 813 (2013)
26. Lavin-Lopez M del P et al. *Indus. Eng. Chem. Res.* **55** 12836 (2016)
27. Yu H et al. *Sci. Rep.* **6** 36810 (2016)
28. Pendolino F, Armata N *Graphene Oxide in Environmental Remediation Process* (Cham: Springer, 2017)
29. Wan Z et al. *Adv. Mater. Technol.* **3** 1700315 (2018)
30. Lerf A et al. *J. Phys. Chem. B* **102** 4477 (1998)
31. Hofmann U, Holst R *Berichte Deutschen Chem. Gesellschaft A, B* **72** 754 (1939)
32. Szabó T et al. *Chem. Mater.* **18** 2740 (2006)
33. Ruess G *Monatshefte Chemie* **76** 381 (1947)
34. Nakajima T, Mabuchi A, Hagiwara R *Carbon* **26** 357 (1988)
35. Pei S, Cheng H-M *Carbon* **50** 3210 (2012)
36. Gómez-Navarro C et al. *Nano Lett.* **10** 1144 (2010)
37. López-Díaz D et al. *Coat. World* **10** 524 (2020)
38. Bagri A et al. *Nat. Chem.* **2** 581 (2010)
39. Ju H-M et al. *Mater. Lett.* **64** 357 (2010)
40. Agarwal V, Zetterlund P B *Chem. Eng. J.* **405** 127018 (2021)
41. Wei Z et al. *Science* **328** 1373 (2010)
42. Su Y et al. *Nano Res.* **6** 842 (2013)
43. Stankovich S et al. *Carbon* **45** 1558 (2007)
44. Gilje S et al. *Nano Lett.* **7** 3394 (2007)
45. Ekiz O O et al. *ACS Nano* **5** 2475 (2011)
46. Voiry D et al. *Science* **353** 1413 (2016)
47. Prezioso S et al. *Langmuir* **28** 5489 (2012)
48. Cote L J et al. *J. Am. Chem. Soc.* **131** 11027 (2009)
49. Cançado L G et al. *Nano Lett.* **11** 3190 (2011)
50. Malinský P et al. *Phys. Chem. Chem. Phys.* **19** 10282 (2017)
51. Kwon S-N et al. *Organic Electron.* **34** 67 (2016)
52. Huh S H et al. *J. Korean Phys. Soc.* **59** 3428 (2011)
53. Yang Y et al. *RSC Adv.* **9** 3597 (2019)
54. Blanton T N, Majumdar D *Powder Diffraction* **28** 68 (2013)
55. Aslam S, Mustafa F, Ashfaq Ahmad M *Ceramics Int.* **44** 6823 (2018)
56. Gao X, Jang J, Nagas S *J. Phys. Chem. C* **114** 832 (2010)
57. Chua C K, Pumera M *Chem. Commun.* **52** 72 (2016)
58. Thakur S, Karak N *Carbon* **94** 224 (2015)
59. Qiu L et al. *Nat. Commun.* **3** 1241 (2012)
60. Zhang J et al. *Chem. Commun.* **46** 1112 (2010)
61. Zhu C et al. *ACS Nano* **4** 2429 (2010)
62. Thakur S, Karak N *Carbon* **50** 5331 (2012)
63. Lingaraju K et al. *Biotechnol. Rep. Amst* **24** e00376 (2019)
64. Gao W et al. *Nat. Chem.* **1** 403 (2009)
65. Faucett A C, Mativetsky J M *Carbon* **95** 1069 (2015)
66. Ghadim E E et al. *Appl. Surf. Sci.* **301** 183 (2014)
67. Pei S, Cheng H-M *Carbon* **50** 3210 (2012)
68. Tu N D K et al. *Chem. Mater.* **27** 7362 (2015)
69. Demazeau G *J. Mater. Chem.* **9** 15 (1999)
70. Eda G, Fanchini G, Chhowalla M *Nat. Nanotechnol.* **3** 270 (2008)
71. Pei S, Cheng H-M *Carbon* **50** 3210 (2012)
72. Gao W et al. *Nat. Chem.* **1** 403 (2009)
73. Cao G et al. *Opto-Electron. Adv.* **1** 18001201 (2018)
74. Cao G et al. *ACS Appl. Mater. Interfaces* **11** 20298 (2019)
75. Jiang H-B et al. *Adv. Funct. Mater.* **24** 4595 (2014)
76. Tran T X et al. *ACS Appl. Mater. Interfaces* **10** 39777 (2018)
77. Gao W et al. *Nat. Nanotechnol.* **6** 496 (2011)
78. Li X et al. *Nat. Commun.* **6** 6984 (2015)
79. Yang C-R, Tseng S-F, Chen Y-T *Appl. Surf. Sci.* **444** 578 (2018)
80. Smirnov V A et al. *High Energy Chem.* **45** 57 (2011)
81. Smirnov V A et al. *Nanotechnol. Russ.* **7** 156 (2012)
82. Plotnikov V G et al. *High Energy Chem.* **45** 411 (2011)
83. Williams G, Seger B, Kamat P V *ACS Nano* **2** 1487 (2008)
84. Williams G, Kamat P V *Langmuir* **25** 13869 (2009)
85. Shul'ga Y M et al. *High Energy Chem.* **46** 117 (2012)
86. Vasilets V N et al. *High Energy Chem.* **52** 14 (2018)
87. Zhao X et al. *Appl. Phys. Lett.* **98** 121905 (2011)
88. Zhou Y et al. *Adv. Mater.* **22** 67 (2010)
89. Trusovas R et al. *Carbon* **52** 574 (2013)
90. Evlashin S A et al. *Adv. Mater. Interfaces* **5** 1800737 (2018)
91. Orekhov N D et al. *Carbon* **191** 546 (2022)
92. Thekkekara L V et al. *Appl. Phys. Lett.* **107** 031105 (2015)
93. Hun S ed S Michailov (InTech, 2011)
94. Arul R et al. *Carbon* **99** 423 (2016)
95. Petridis C et al. *Appl. Phys. Lett.* **102** 093115 (2013)
96. Lima B S de et al. *Appl. Surface Sci.* 144808 (2019)
97. Jiang H-B et al. *ACS Appl. Mater. Interfaces* **10** 18416 (2018)
98. Pérez L A, Bajales N, Lacconi G I *Appl. Surf. Sci.* **495** 143539 (2019)
99. Wan Z et al. *Carbon* **141** 83 (2019)
100. Guo L et al. *J. Phys. Chem. C* **116** 3594 (2012)
101. Evlashin S et al. *ACS Appl. Mater. Interfaces* **8** 28880 (2016)
102. Al-Gaashani R et al. *Ceramics Int.* **45** 14439 (2019)
103. Kovtun A et al. *Carbon* **143** 268 (2019)
104. Kolesov B A *Prikladnaya KR-Spektroskopiya* (Applied Raman Spectroscopy) (Novosibirsk: Izd. SO RAN, 2018)

105. Babaev A A et al. *Opt. Spectrosc.* **125** 1014 (2018); *Opt. Spektrosk.* **125** 820 (2018)
106. Childres I et al., in *New Developments in Photon and Materials Research* (Ed. J I Jang) (New York: Nova Science Publ., 2013) p. 403
107. Eigler S, Dotzer C, Hirsch A *Carbon* **50** 3666 (2012)
108. Strankowski M et al. *J. Spectrosc.* **2016** 1 (2016)
109. Kudin K N et al. *Nano Lett.* **8** 36 (2008)
110. Rodriguez R D et al. *Carbon* **151** 148 (2019)
111. Chen H-Y et al. *Chem. Phys.* **430** 13 (2014)
112. Deng N-Q et al. *Carbon* **109** 173 (2016)
113. Yung K C et al. *J. Appl. Phys.* **113** 244903 (2013)
114. Bobrinetskiy I I et al. *Mater. Lett.* **187** 20 (2017)
115. Kasischke M et al. *Appl. Surf. Sci.* **445** 197 (2018)
116. Guan Y C et al. *Sci. Rep.* **6** 28913 (2016)
117. Pei S et al. *Carbon* **48** 4466 (2010)
118. Tao Y et al. *Appl. Phys. A* **106** 523 (2012)
119. Mukherjee R et al. *ACS Nano* **6** 7867 (2012)
120. Sokolov D A et al. *Carbon* **53** 81 (2013)
121. Ma B et al. *Phys. Chem. Chem. Phys.* **21** 10125 (2019)
122. Strong V et al. *ACS Nano* **6** 1395 (2012)
123. Murastov G et al. *Biosensors Bioelectron.* 112426 (2020)
124. Kuhnel D T et al. *Adv. Mater. Technol.* **4** 1800232 (2019)
125. Muttaqin et al. *J. Mater. Sci.* **52** 749 (2017)
126. Evlashin S et al. *ACS Appl. Mater. Interfaces* **8** 28880 (2016)
127. Hosseindokht Z et al. *Superlatt. Microstruct.* **140** 106470 (2020)
128. Prakash V et al. *Analyst* **144** 3297 (2019)
129. Lin J et al. *Nat. Commun.* **5** 5714 (2014)
130. Romero F J et al. *Nanomaterials* **8** (2018)
131. Yang D, Bock C *J. Power Sources* **337** 73 (2017)
132. Liu C et al. *Carbon* **166** 138 (2020)
133. Ibrahim Y O et al. *Ceramics Int.* **46** 444 (2020)
134. Ran P et al. *J. Mater. Chem. A* **6** 16430 (2018)
135. Liu C et al. *Nano Lett.* **10** 4863 (2010)
136. Pandolfo A G, Hollenkamp A F *J. Power Sources* **157** 11 (2006)
137. Ghoniem E et al. *J. Power Sources* **324** 272 (2016)
138. El-Kady M F et al. *Science* **335** 1326 (2012)
139. Borenstein A et al. *J. Mater. Chem. A* **6** 20463 (2018)
140. Stoller M D et al. *Nano Lett.* **8** 3498 (2008)
141. Romero F J et al. *Sensors Actuators A* **274** 148 (2018)
142. Meng F-L, Guo Z, Huang X-J *TrAC Trends Analyt. Chem.* **68** 37 (2015)
143. Guo L et al. *Sci. Rep.* **8** 4918 (2018)
144. Cui S et al. *Anal. Chem.* **86** 7516 (2014)
145. Bhati V S et al. *ACS Appl. Mater. Interfaces* **10** 11116 (2018)
146. Drmosh Q A et al. *Sensors Actuators B* **290** 666 (2019)
147. Lai T et al. *Electrochim. Acta* **138** 48 (2014)
148. Han B et al. *Sensors Actuators B* **270** 500 (2018)
149. Silipigni L et al. *J. Instrum.* **15** C04006 (2020)
150. An J et al. *ACS Appl. Mater. Interfaces* **9** 44593 (2017)
151. Searle A, Kirkup L *Physiol. Meas.* **21** 271 (2000)
152. He Y et al. *IEEE Photon. Technol. Lett.* **28** 1996 (2016)
153. Romero F J et al. *Nanomaterials* **9** 897 (2019)
154. Wang Q et al. *Appl. Phys. Lett.* **112** 133902 (2018)
155. Han B et al. *Adv. Mater.* **31** 1806386 (2019)
156. Zhang T-Y et al. *Appl. Phys. Lett.* **111** 121901 (2017)
157. Bi H et al. *Nanoscale* **5** 9123 (2013)
158. Sang W et al. *Macromol. Mater. Eng.* **302** 1700239 (2017)
159. Low M J et al. *Appl. Surf. Sci.* **526** 146647 (2020)
160. Zheng X et al. *Nat. Commun.* **6** 8433 (2015)
161. Zheng X et al. *J. Phys. D* **50** 074003 (2017)
162. Bi Y-G et al. *ACS Photon.* **1** 690 (2014)
163. Wei J et al. *Opt. Lett.* **42** 911 (2017)
164. Yuan Q, Lin C-T, Chee K W A *APL Mater.* **7** 030901 (2019)
165. Huang L et al. *Carbon* **49** 2431 (2011)
166. Malinský P et al. *EPJ Web Conf.* **167** 04010 (2018)
167. de Lima B S, Bernardi M I B, Mastelaro V R *Appl. Surf. Sci.* **506** 144808 (2020)
168. Malek Hosseini S M B et al. *Appl. Surf. Sci.* **427** 507 (2018)
169. Das S R et al. *Nanoscale* **8** 15870 (2016)
170. Romero F J et al. *Sensors Actuators B* **287** 459 (2019)
171. Watanabe A et al. *Proc. SPIE* **10906** 1090612 (2019)
172. Komarov I A et al., in *Metodologicheskie Aspekty Skaniruyushchei Zondovoi Mikroskopii* (Eds T A Kuznetsov et al.) (Minsk: Inst. Teplo- i Massoobmena im. A V Lykova, 2018) p. 353
173. Kavinkumar T, Shobin L R, Manivannan S *J. Alloys Compd.* **784** 301 (2019)
174. Timofeeva T E, Nikolaev D V, Timofeev V B *Innovatsion. Nauka* (7) 18 (2019)
175. Cutroneo M et al. *Vacuum* **165** 134 (2019)
176. Tian Y et al. *J. Mater. Chem. A* **3** 11294 (2015)